DOI: https://doi.org/10.52756/ijerr.2023.v36.027 *Int. J. Exp. Res. Rev.*, **Vol. 36: 285-310 (2023)**

Original Article | *Peer Reviewed* | *Open Access*

International Journal of Experimental Research and Review (IJERR)
© Copyright by International Academic Publishing House (IAPH)
ISSN: 2455-4855 (Online)
www.iaph.in

High Purity Orbital Angular Momentum Modes Reconfiguration Using Uniform Circular Array Antenna to Enhance Channel Capacity and Spectral Efficiency

Rakhee[1], Rajesh Bhadada[1] and Usha[2*]

[1]Department of Electronics and Communication Engineering, MBM University, Jodhpur, India;
[2]Department of Electronics and Communication Engineering, Jodhpur National University, Jodhpur, India
E-mail/Orcid Id:
R, rakhee1.dhaiya@gmail.com, https://orcid.org/0009-0004-3122-8718; *RB,* rajesh_bhadada@rediffmail.com;
U, usha.meel05@gmail.com, https://orcid.org/0009-0009-7924-6911

Article History:
Received: 9th Oct., 2023
Accepted: 15th Dec., 2023
Published: 30th Dec., 2023

Keywords:
EFPDP, NRP, OAM, Observational Distance, UCA Antenna factor, UCA elements, UCA radius

How to cite this Article:
Rakhee, Rajesh Bhadada and Usha (2023). High Purity Orbital Angular Momentum Modes Reconfiguration Using Uniform Circular Array Antenna to Enhance Channel Capacity and Spectral Efficiency. *International Journal of Experimental Research and Review*, *36*, 285-310.
DOI:
https://doi.org/10.52756/ijerr.2023.v36.027

Abstract: Technology based on OAM (orbital angular momentum) has great potential for enhancing the bandwidth efficiency of telecommunication systems. Although OAM waves are orthogonal, it is possible to multiplex various modes within a single frequency channel. Significantly, the overall spectrum efficiency, as well as channel capacity, can be improved. Multiple users can share the same frequency channel by using orthogonal modes, which eliminates the requirement for extra resources like time and frequency. This research uses MATLAB code to derive a uniform circular array (UCA) antenna factor under the cylindrical coordinate system. This factor is used to illustrate the array antenna's electric field to generate OAM waves or radio waves that carry the OAM mode. OAM modes can be reconfigured for the no. of UCA elements (N) needed to generate a ripple-free radiation pattern based on the UCA antenna factor. Additionally, the significance of UCA radius and observational distance (the field plane-UCA plane gap) on the phase distribution and radiation pattern from OAM mode 1 to 5 is graphically evaluated and optimized. The MATLAB simulations compute the electric field phase distribution pattern (EFPDP) and normalized radiation pattern (NRP) at 76 GHz. The method predicts the peak, side lobes, and comparable radiation patterns of the radiation pattern, offering an effective means of optimizing OAM modes and analysing trade-offs.

Introduction

Orbital and spin angular momentum are the two types of angular momentum carried by electromagnetic (EM) waves. The momentum produced by the electrons' spin equals SAM, while the momentum produced by their circular motion around the nucleus is equal to OAM. The idea of an optical vortex, which is created when the planes of the constant phase of the electric and magnetic vector fields form a corkscrew or helicoid (helix-shaped structure flowing in the direction of propagation), was initially used by scientists Allen et al. to illustrate the concept of OAM. OAM beams are electromagnetic waves with a helical phase structure that are represented by the phase term exp(ilφ). The azimuthal angle around the propagation axis is denoted by φ, and *l* is an integer known as the topological charge (OAM mode order). It represents the number of wavefront twists present at each wavelength. Laguerre-Gaussian (LG) waves are a type of helically phased beam analogous to other special OAM waves. Their radial intensity distributions could obtain a relevant description. A radio beam with OAM is an LG beam. The cylindrical LG modes can be used to describe beams carrying orbital angular momentum since they have an explicit phase factor exp(ilφ) (Turnbull et al., 1996). The goal of fifth-generation (5G), the current network standard, is to perform 100 times better than 4G networks. 5G would provide high data throughput, low latency, and superior service quality (Albreem, 2015). To satisfy mobile communication demands, an efficient wireless access technique that can amplify wireless area throughput without increasing bandwidth is needed. Radio frequency OAM waves have drawn a lot of

*Corresponding Author: usha.meel05@gmail.com

Table 1. Various studies along with drawbacks and solutions

Reference	Title of the paper	Addressed drawback	Solutions
Fang and Henderson, 2019a	Uniform Millimetre-Wave OAM Dipole Array with Reflector	Electromagnetic compatibility issue due to unwanted backward radiation	By adding a planar metallic reflector
Hasan et al., 2021	Beam divergence reduction of vortex waves with a tailored lens and a tailored reflector	Large beam divergence	By using tailored lenses
Hasan et al., 2020	Evolution of different phased array approaches for orbital angular momentum beam steering	Misalignment between OAM transmitter and receiver	By steering the vortex beam
Chen et al., 2018	Orbital angular momentum generation and detection by geometric-phase-based meta-surface	Beam divergence	Employing large frequencies such as 60 GHz
Qu et al., 2020	Optimal power allocation algorithm for multi-mode OFDM-OAM communications systems in multi-path channels	Multipath Fading	A robust optimal power allocation algorithm for multi-mode OFDM-OAM communications

recognition as a solution to the subject. Using Beam-carrying OAM (OAM waves) instead of traditional plane waves is one possible way to better use the 5G networks. OAM waves can offer additional flexibility because the generated OAM modes are inherently orthogonal. This indicates that because OAM wave modes are orthogonal, they can be multiplexed in the same frequency channel (Cheng et al., 2019). Consequently, transmitting data in many modes ensures that the available bandwidth is utilized to its fullest extent. Therefore, it is predicted that integrating OAM beams into the next generation of telecommunication systems will potentially improve services like high spectrum efficiency, improved data rates, and highly secure communication. OAM beams have not been extensively studied in the radio domain for telecommunication systems. Thus, the various aspects of OAM wave optimization in the radio domain are covered in this paper.

Literature Review

OAM beams can be generated through an array of methods, including metasurface, parabolic reflector antennas (PRA), and spiral phase plates (SPP). The inability to generate numerous modes in SPP, the need for a large aperture size in PRA, and the significant absorption loss on the metasurface are the main disadvantages of these techniques (Isakov et al., 2020; Xu et al., 2020; Yu et al., 2016). The method most commonly employed to generate OAM modes is the UCA because of its adaptability, compatibility, and simplicity in fabrication. Using the UCA antenna, it is possible to work at lower, intermediate, and higher frequencies (Bai et al., 2014), resulting in uncomplicated designs with lightweight, compact structures. Additionally, several modes can be generated simultaneously by designing multiple layers within the same structure. With UCA, it is simple to implement multiple OAM-mode reconfigurability to generate various OAM-modes while maintaining a complete, compact, and simple structure. Consequently, UCA has drawn much interest and has been observed to be an excellent medium for producing OAM beams. As shown in Table 1, most studies concentrate on specific OAM-related problems (such as mode divergence, multipath fading, etc.). In contrast, very few efforts have been made to utilize UCA to generate improved OAM modes.

In this research, the UCA antenna, which is made up of dipole antenna elements, is used to generate radio beams carrying OAM. The dipole antenna is appropriate for wideband millimetre-wave transmission due to its greater bandwidth and radiation efficiency. On the other hand, planar dipole UCAs can produce both forward and backward emission (Fang et al., 2017). Based on MATLAB simulation, UCA radius (a), the number of UCA elements (N), and observational distance (z) that are related to the OAM beam's radiation performance are examined and improved. Lastly, based on the simulation of electromagnetic wave propagation, improved OAM modes are suggested to mitigate issues with OAM beams,

DOI: https://doi.org/10.52756/ijerr.2023.v36.027

such as mode divergence and misalignment (while keeping good mode purity).

Methodology

A phase shift of $2\pi l/N$ between adjoining elements and equal power feeding to each element is required to generate OAM mode l using N-element UCA (Bai et al., 2014). Figure 2 and its corresponding attributes represent a N-element UCA in the cylindrical coordinate system. Equation (1) represents its accumulated E-field distribution at field point (y, φ, z).

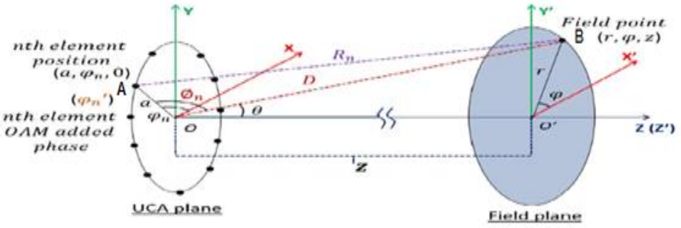

Figure 1. Illustration of UCA array in cylindrical coordinates.

$$E(r,\varphi,z) = \textstyle\sum_{n=1}^{N} \; a_n.\frac{e^{-iKR_n}}{R_n}.\exp\left[-i(l\,.\varphi_n' + \;\varphi_{0n}{}'\,)\right]\ldots.\;(1)$$

Where,

- Distance between the field point and the array element (source point) = Rn
- The amplitude of each element (in an ideal UCA, all elements are identical, so the amplitude can be normalized to unity) = a_n
- Order of OAM mode = l
- Phase added to each element of UCA antenna is OAM = $l.\varphi_n{}' + \varphi_{0n}{}'$
- phase shift between adjoining elements= $\varphi_n{}'$
- Intrinsic phase of each element (as all elements should have the same intrinsic phase in an ideal UCA, so for the purpose of simplicity, it might be adjusted to zero) = $\varphi_{0n}{}'$
- Phase term for the element's physical position =ϕn = $2\pi n/N$
- Wave number = k = $2\pi/\lambda$.
- UCA radius (measure of UCA size) = a
- Isotropic radiator $=e{-}ikR_n/R_n$= this term indicates that the individual dipole antenna element in the UCA is represented by an isotropic (physically identical in all directions) radiator.
- Distance between the UCA plane and field plane =Z
- The UCA antenna factor's divergence angle = θ = $sin^{-1}(r/\sqrt{z^2} + r^2)$
- Radius of field plane = r
- Distance between field point 'B' to the UCA center point 'O' = D

Equation (2) provides the OAM–UCA factor's summing form.

$$E(r,\varphi,z) = \textstyle\sum_{n=1}^{N} \frac{e^{-iKR_n}}{R_n}.\exp\left[-i(l\,.\varphi_n'\,)\right] \ldots\ldots\ldots..(2)$$

Here the exp($-il\varphi$n') is the OAM phase factor term, which contributes to the twisted phase distribution along the direction of transmission. Based on equations (1) and (2), which serve as a recommendation, a MATLAB code has been generated to provide improved OAM modes through UCA antenna.

Parametric Analysis

When an OAM mode has an integer-required topological charge, it is referred to as the pure OAM mode. One property of OAM beams that directly impacts the dependability of data transfer is mode purity. To guarantee that the modes are orthogonal to one another, it is crucial to generate OAM waves with mode purity (Li et al., 2014). In order to effectively use the OAM system for telecommunication and to partially overcome the limits of the OAM wave for real-world applications, the purity of OAM modes must be taken into account. The impact of modifying essential factors such as the observational distance (z), UCA radius (a), and number of UCA elements (N) must be taken into account and investigated in order to design a UCA for the intended OAM mode generation. A flow diagram in Figure 2 provides an overview of the simulation procedure.

Approximation and analysis of UCA elements number for ripple-free OAM modes

An array of identical linked antennas evenly placed around a circle is called a uniform circular array (UCA), and it acts as a single antenna to produce OAM beams. Here, a single antenna is referred to as a UCA element, and the number of UCA elements collectively is indicated by N (Mohammadi et al., 2014). The primary essential for producing OAM mode l by the use of N-element UCA is displayed in (3).

$$N \geq 2\,|l| + 1 \ldots\ldots\ldots\ldots\ldots\ldots\ldots\ldots\ldots\ldots\ldots\ldots\ldots\; (3)$$

Using MATLAB simulation, NRP and EFPDP have been generated for various numbers of UCA elements for modes 1 through 5. Verification of performance has been made possible by NRP and EFPDP.

(a) Analysis of 'N' for OAM Mode 1

On the basis of equation (3), simulations have been started from N= 4 for OAM mode 1 in order to find the minimal N required to achieve ripple-free OAM modes. At a fixed observation distance of 20λ and a fixed UCA radius of 1.2λ (where λ represents the wavelength in the vacuum of the UCA operating frequency), simulations have been conducted for N=4, 6, 7, 8, and 9 for OAM

DOI: https://doi.org/10.52756/ijerr.2023.v36.027

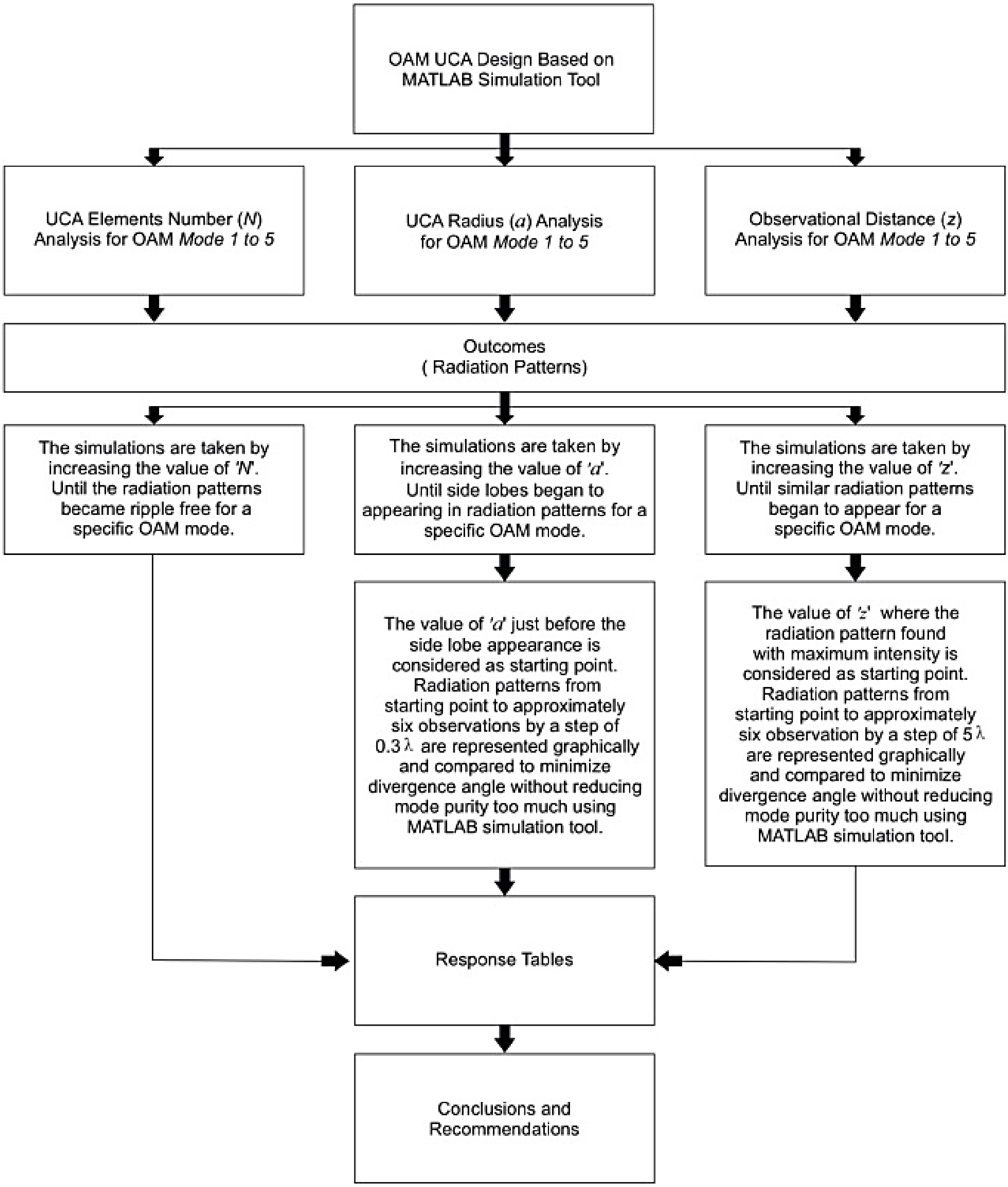

Figure 2. The operational outflow of the simulation framework.

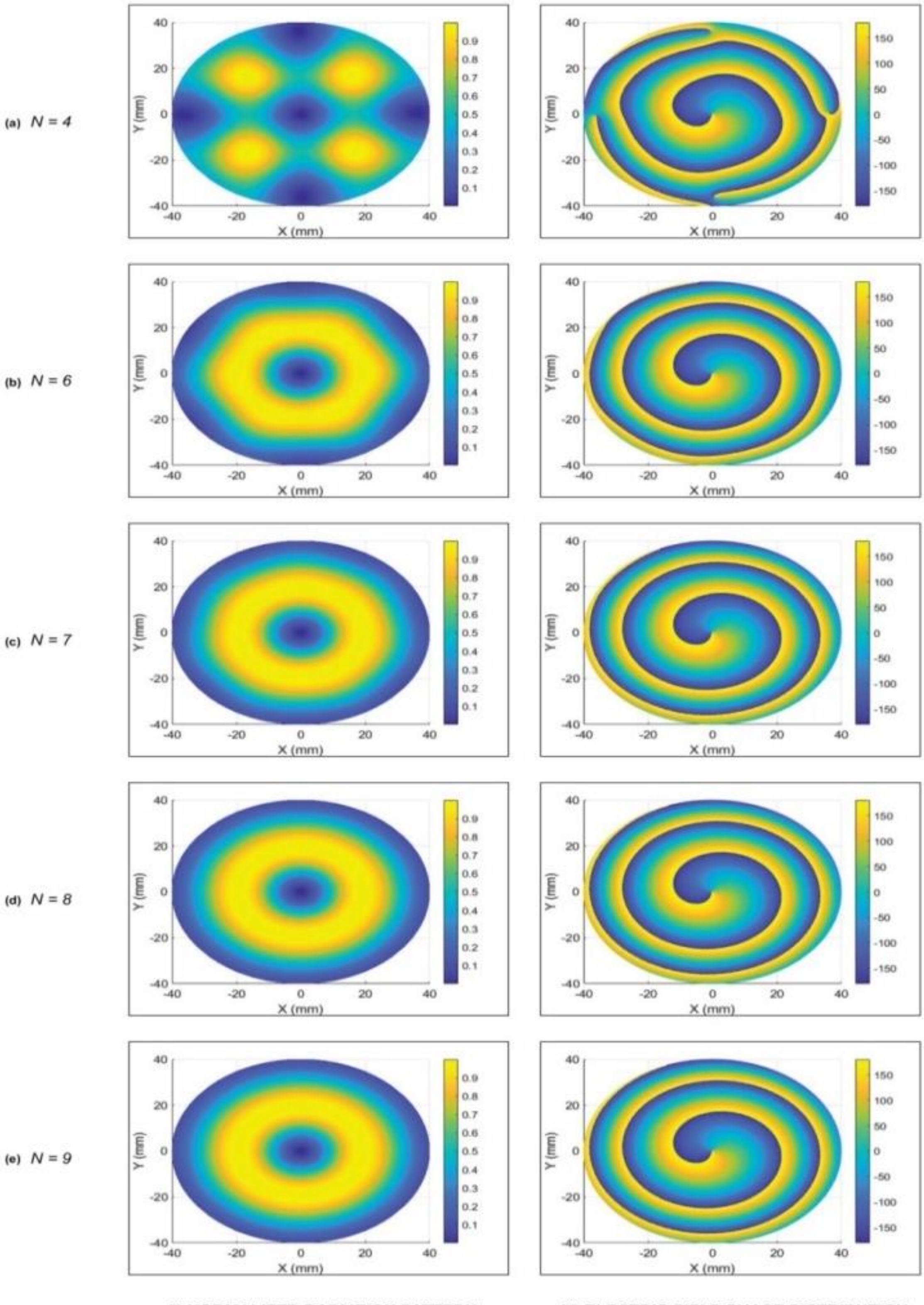

Figure 3. NRP and EFPDP at distinct UCA elements for OAM mode 1.

mode 1. An annular or circular intensity profile, which is an absolute configuration of NRP, does not form at N=4, as shown in Figure 3(i)(a). There are ripples in NRP at N=7 and N=6 (wavy fluctuations in the yellow ring in Figs. 3(i)(c) and 3(i)(b) showing the presence of ripple). A near-perfect structure (doughnut-shaped yellow ring) of NRP is obtained because all ripples are eliminated at N=8 and N=9. Figures 3(i)(d) and 3(i)(e) provide illustrations of it. With reference to Figure 3(ii)(a), a single twisted EFPDP is formed at N=4 in the central region, confirming that all UCAs, provided they satisfy the basic essential, can generate OAM mode 1. However, wavy spirals (ripples) in the phase distribution pattern were discovered in the EFPDP. As N increases, spiral waviness diminishes. A modest spiral form of EFPDP is seen at N=8 (Figure 3(ii)(d)). Thus, it can be concluded that N=8 is the minimum vital no. of array elements needed to provide ripple-free OAM mode 1.

DOI: https://doi.org/10.52756/ijerr.2023.v36.027

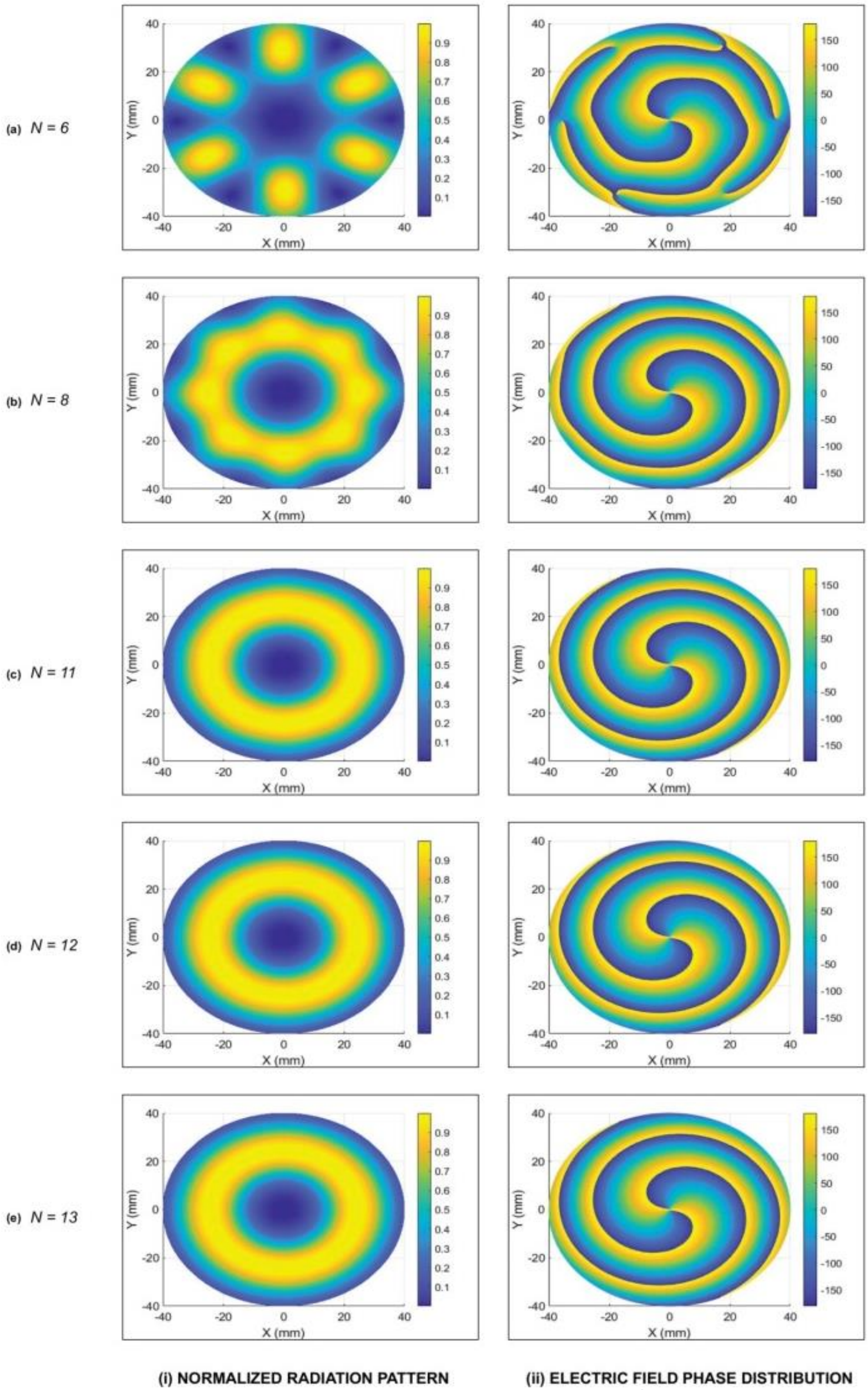

Figure 4. NRP and EFPDP at distinct UCA elements for OAM mode 2.

(b) Analysis of 'N' For OAM Mode 2

For OAM mode 2, simulations have been begun from *N*= 6 based on eq. (3). For OAM mode 2 generation, simulations have been conducted for UCA elements 6, 8, 10, 11, 12, and 13 at a fixed UCA radius of 1.7λ and a fixed observation distance of 21λ.

An annular (or circular) intensity profile of NRP did not form at N=6 (Figure 4(i)(a)), which was the absolute configuration. Wavy fluctuations were observed in NRP at N=8 and N=11 (Figures 4(i)(b) and 4(i)(c)). Due to the total removal of ripples, a nearly ideal structure (doughnut-shaped yellow ring) of NRP was found at N=12 and N=13 (Figure 4(i)(d) and 4(i)(e)). In the middle area, double twisted EFPDP was formed at N=6, as shown in Figure 4(ii)(a). However, wavy EFPDP spirals were discovered. As N increases, spiral waviness diminishes. A complete spiral form of EFPDP was seen at N=12 (Figure 4(ii)(d)). Thus, it can be concluded that N=12 is the minimum vital no. of array elements needed to provide OAM mode 2 free from ripples.

DOI: https://doi.org/10.52756/ijerr.2023.v36.027

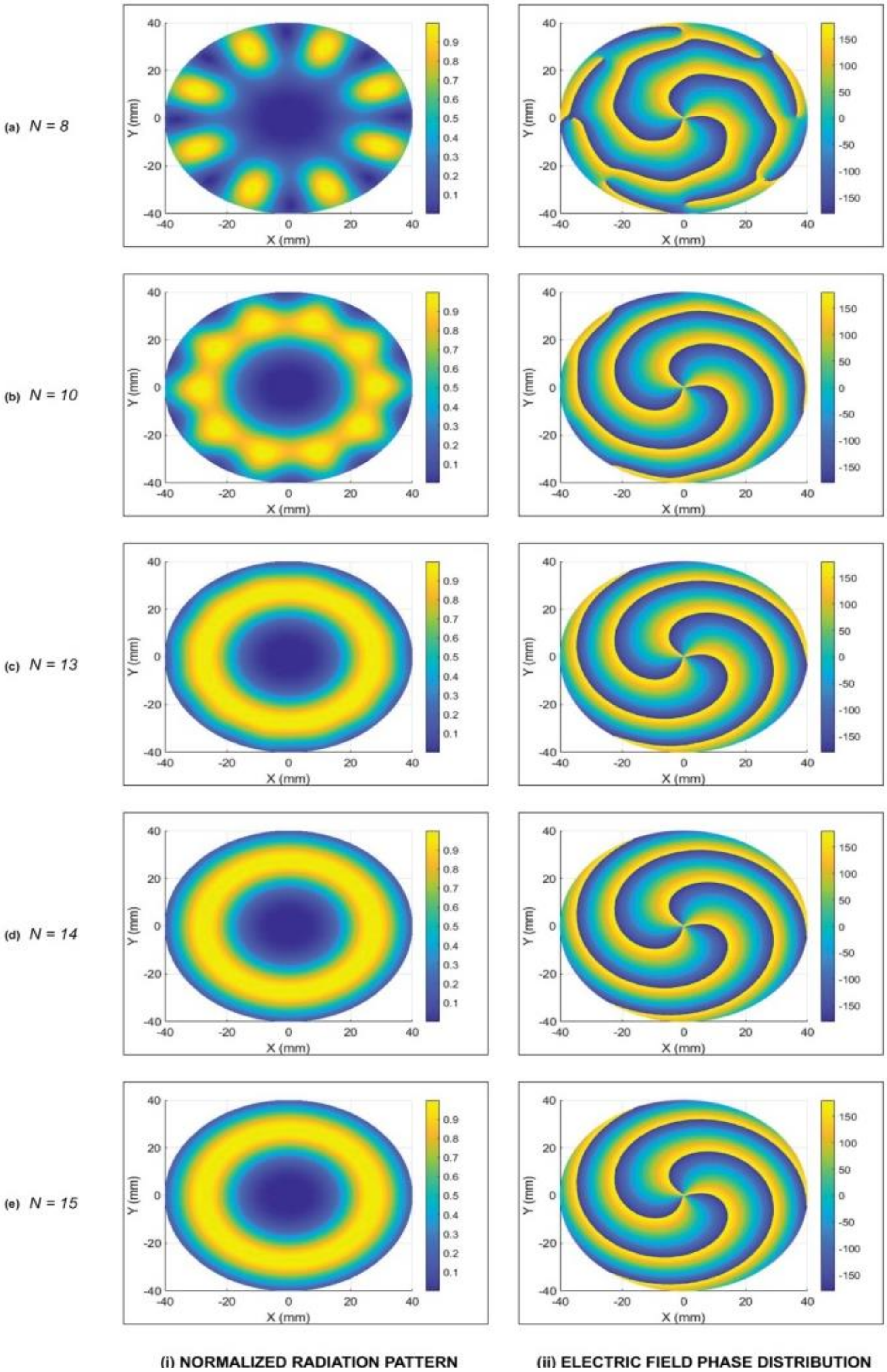

Figure 5. NRP and EFPDP at distinct UCA elements for OAM mode 3.

(c) Analysis of ‘N’ For OAM Mode 3

For OAM mode 3, simulations have been initiated from *N*= 8 based on equation (3). For OAM mode 3 generation, simulations have been conducted for UCA elements 8, 10, 13, 14, and 15 elements at a fixed observational distance of 22λ and a fixed radius of 2.2λ. An annular (or circular) intensity profile of NRP did not form at N=8, as indicated in Figure 5(i)(a). Ripples were discovered in NRP at N=10 and N=13 (Figures 5(i)(b) and 5(i)(c)). Due to the total removal of ripples, near-ideal structures (doughnut-shaped bright yellow NRPs) were found at N=14 and N=15 (Figures 5(i)(d) and 5(i)(e). In the central area, triple twisted EFPDP was formed at N=8, as shown in Figure 5(ii)(a). However, wavy EFPDP spirals were discovered. As N increases, spiral waviness diminishes. A complete spiral form of EFPDP was achieved at N=14 (Figure 5(ii)(d)). Thus, it can be concluded that N=14 is the essential minimum no. of array elements needed to provide ripple-free OAM mode 3.

DOI: https://doi.org/10.52756/ijerr.2023.v36.027

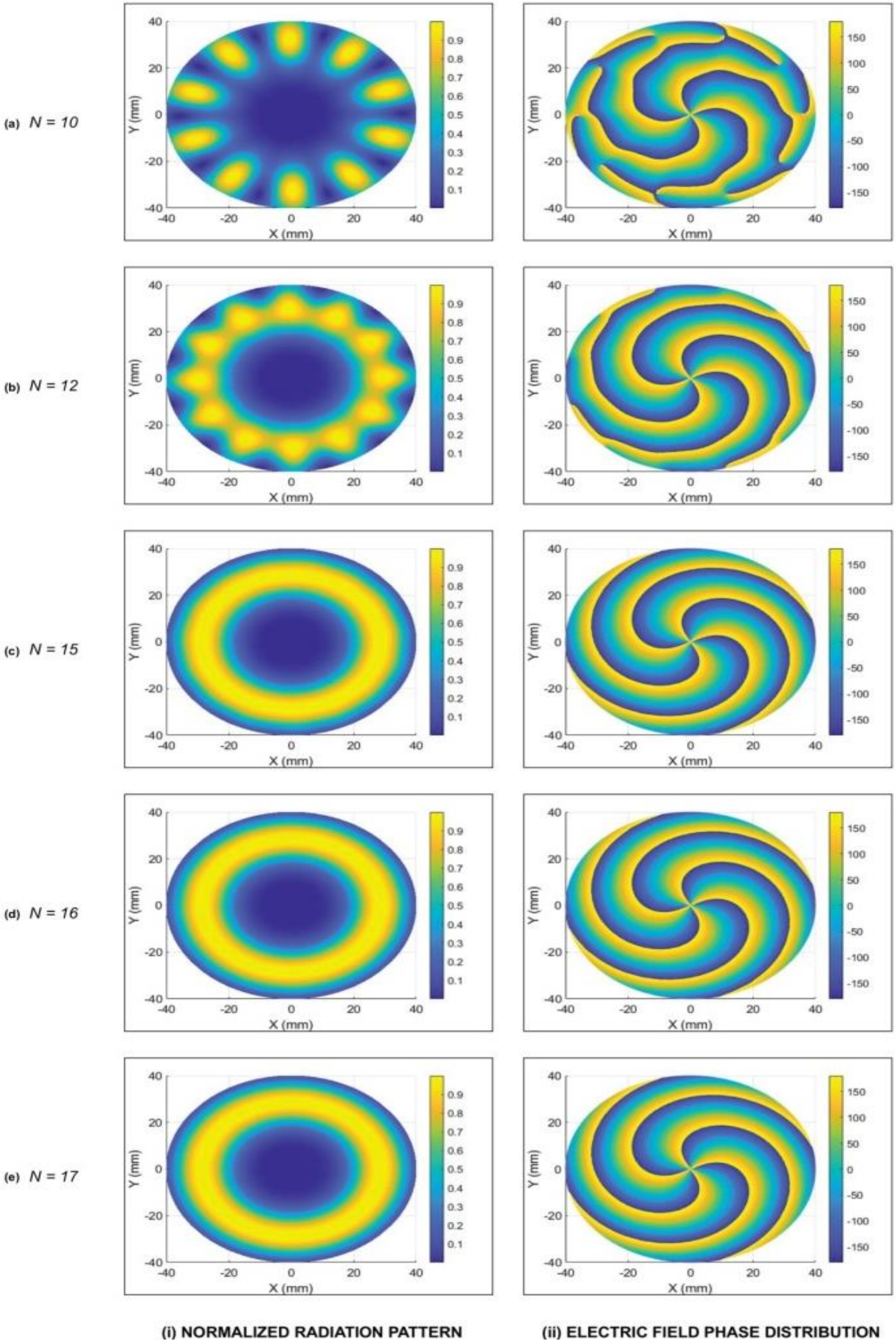

Figure 6. NRP and EFPDP at distinct UCA elements for OAM mode 4.

(d) Analysis of 'N' For OAM 4

For OAM mode 4, simulations have been initiated from $N = 10$ based on equation (3). For OAM mode 4, simulations have been conducted for 10, 12, 15, 16, and 17 elements, with a fixed UCA radius of 2.7λ and a fixed observation distance of 22λ. The absence of an annular or circular NRP intensity profile was shown at N=10, indicated in Figure 6(i)(a). Wavy fluctuations in the yellow ring were discovered in NRP at N=12 and N=15 (Figures. 6(i)(b) and 6(i)(c)). The near-perfect structure of NRP is attained at N=17 and N=16 as a result of all ripples being completely eliminated (Figure 6(i)(e) and 6(i)(d). Concerning Figure 6(ii)(a)), in the central area, quadruple twisted EFPDP was formed at N=10. However, EFPDP spirals were wavy. As N increases, spiral waviness keeps decreasing. An errorless spiral form of EFPDP was obtained at N=16 (Figure 6(ii)(d)). Thus, it can be concluded that N=16 is the essential minimum no. of array elements needed to provide ripple-free OAM mode 4.

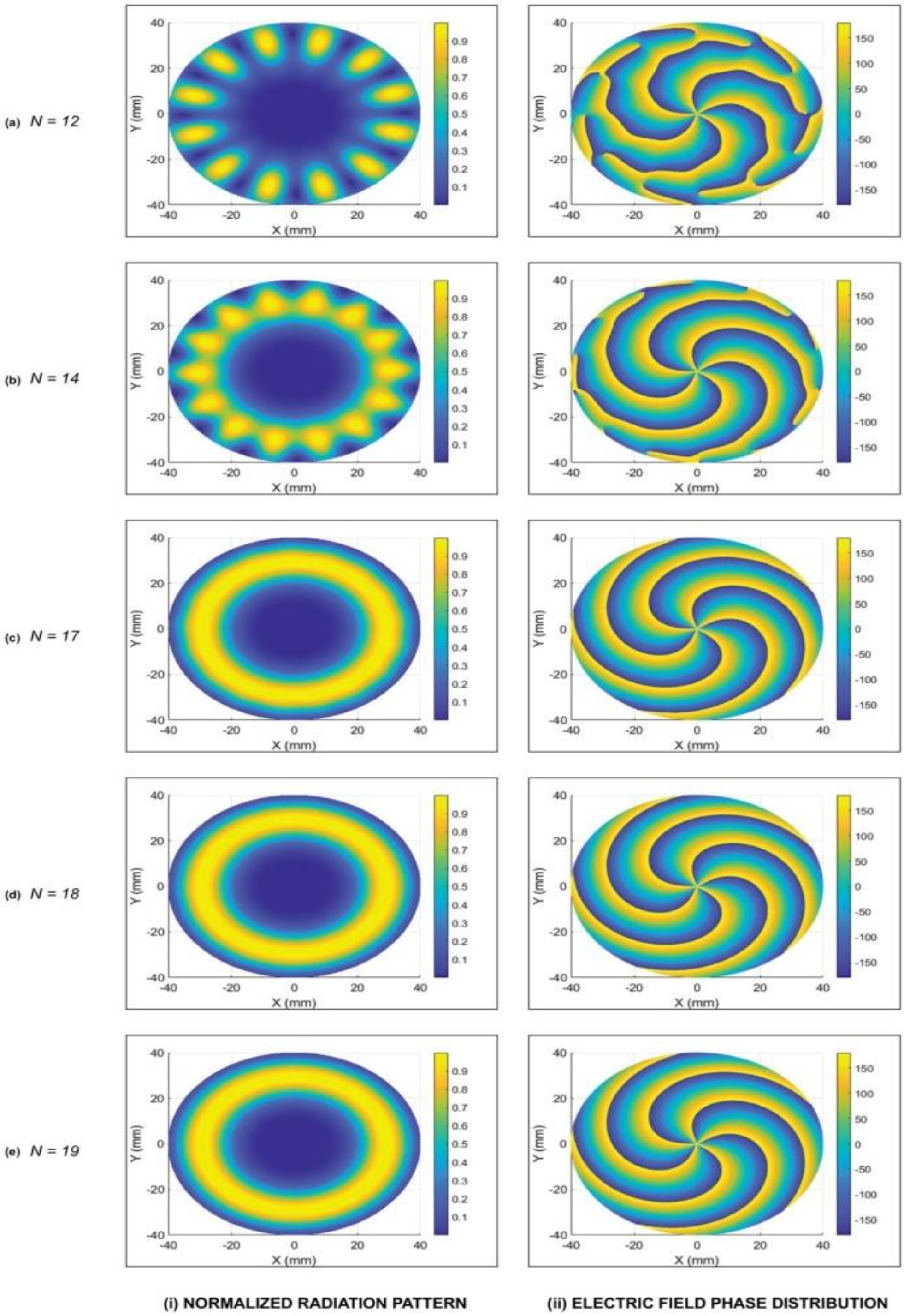

Figure 7. NRP and EFPDP at distinct UCA elements for OAM mode 5.

(e) Analysis of 'N' for OAM 5

For OAM mode 5, simulations have been begun from N= 12 based on eq. (3). For OAM mode 5 generation, simulations have been conducted for N= 12, 14, 17, 18, and 19 at a fixed observation distance of 22λ, with a fixed UCA radius of 3.1λ.

An annular (or circular) intensity profile of NRP does not form at N=12 (Figure 7(i)(a)). Ripples were discovered in NRP at N=14 and N=17 (Figs. 7(i)(b) and 7(i)(c). The total elimination of ripples at N=18 and N=19 resulted in a nearly ideal structure (doughnut-shaped yellow NRP) (Figure 7(i)(d) and 7(i)(e)). Quintuple twisted EFPDP at N=12 was produced in the central region, as shown in Figure 7(ii)(a). However, wavy spirals were discovered in EFPDP. As N increases, spiral waviness diminishes. A complete spiral form of EFPDP was obtained at N=18 (Figure 7(ii)(d)). Thus, it can be concluded that N=18 is the vital minimum no. of array elements needed to provide ripple-free OAM mode 5.

UCA Radius 'a' Approximation and analysis for Optimized OAM Modes

The transmitting antenna array's size is computed by its UCA radius. The OAM beam gets more directed as the transmitting array antenna's radius extends, but inevitably, some side lobes form and the size of the

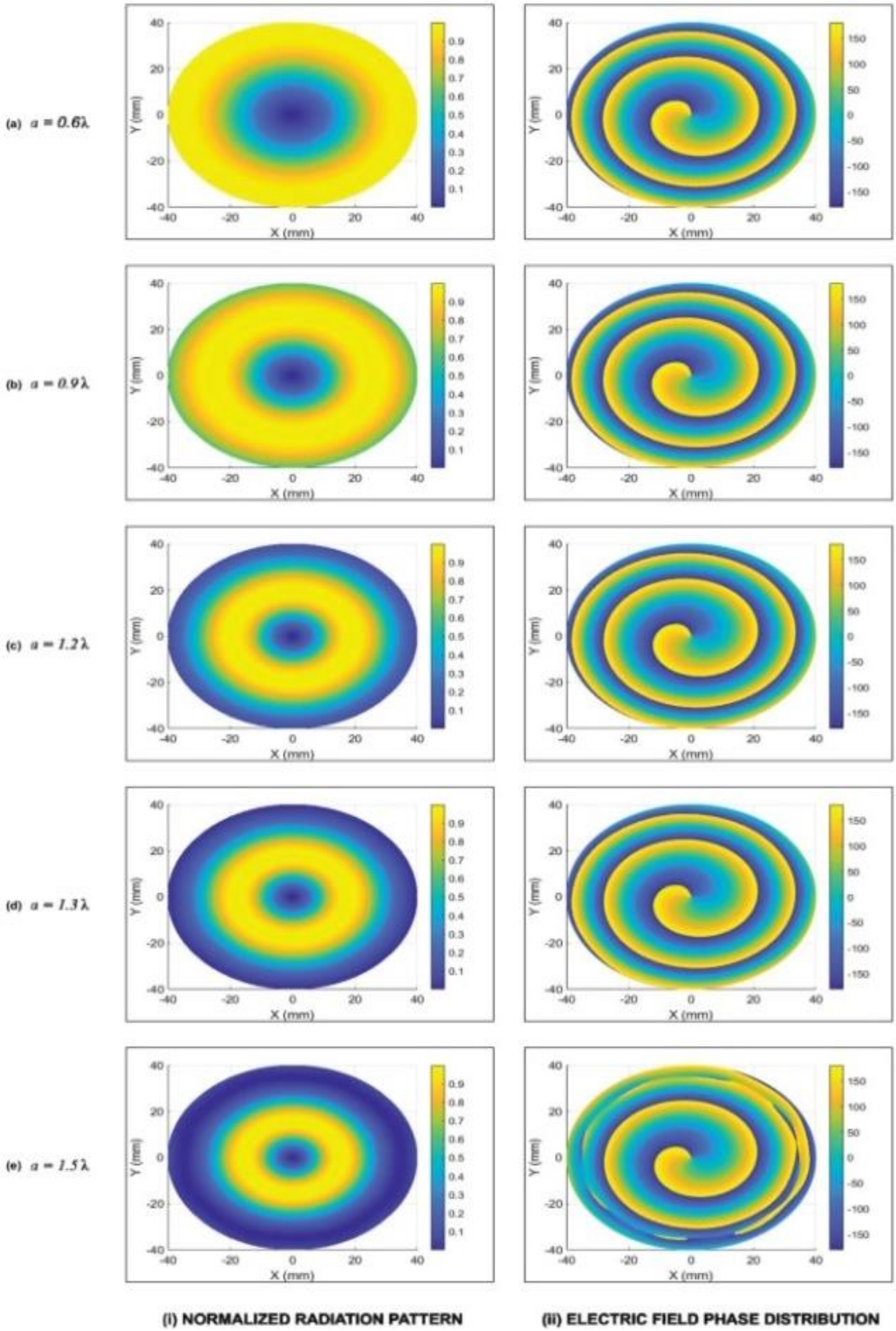

Figure 8. For OAM mode 1, NRP and EFPDP at various UCA radii.

antenna gets bigger. This causes the mode purity to decrease (Li et al., 2014). Mode purity and divergence are incompatible. The impact of variation in UCA radius has been investigated as the next significant factor. Using MATLAB simulation software, a method has been developed to determine the value of UCA radius needed for a certain OAM mode in order to accomplish good mode purity with less mode divergence.

(a) Analysis of UCA Radius for OAM Mode 1

"Radiation patterns free of side lobes are encountered at small antenna radii" (Yao et al., 2017). Thus, for OAM mode 1, at a given observational distance of 20λ, simulations for 0.60λ, 0.90λ, 1.20λ, 1.30λ, and 1.50λ

UCA radii have been conducted. Figures 8(i) and 8(ii) show the NRP and EFPDP for a = 0.60λ, 0.90λ, 1.20λ, 1.30λ, and 1.50λ, respectively. At a = 0.60λ, side lobes were absent from NRP, shown in Figs. 8(i)(a) and Fig 8(ii)(a) showed the perfect single twisted configuration of EFPDP. As the UCA radius was raised and exceeded 1.2, side lobes were seen to emerge in NRP [Figure 8(i)(e)]. The presence of side lobes is shown by the deepest blue colour ring in NRP at a = 1.3λ (Figure 8(i)(d)). In NRP (Figure 8(i)(e)), the outer area of that ring indicates the side lobes at b = 1.5λ. Pattern spiral distortions indicate the appearance of side lobes in EFPDP. Minimal distortions are seen at the outer spiral of the EFPDP at a = 1.3λ (Figure 8(ii)(d)). Visible distortions are seen at the outer spiral of the EFPDP at a = 1.5λ (Figure 8(ii)(e)).

The influence of radius on radiation patterns is examined using a minimum 8-element UCA since N=8 is the smallest number of array elements needed to generate a ripple-free OAM mode 1. It was discovered in the simulation that side lobes did not emerge until a = 1.2λ. Thus, 1.2λ is utilized as the initial value. With a step size of 0.3λ, observations were made up to a = 2.7λ. The outcomes are displayed in Figure 9. The divergence angle corresponding to the smallest UCA radius (a = 1.2λ) occurred at about 26.751 degrees, as indicated by the blue line in Figure 9, and at this radius, there were no side lobes.

A deep curve, indicated by the yellow line, representing a side lobe was discovered at a = 1.5λ. It was found that the divergence angle becomes less as the radius becomes greater. The divergence angle did not considerably decrease after a = 2.1λ, although the amount of side lobes increased. Consequently, it can be concluded that a = 2.1λ, at which a divergence anmode of nearly 16.901 degrees is generated, is considered a good stopping point (shown by the green line in Figure 9) for OAM angle 1.

(b) Analysis of UCA Radius for OAM Mode 2

Since all of the radiation patterns were discovered to be approximately comparable before a =1.1λ, along with no side lobes. So, simulations for OAM mode 2 have been initiated at a =1.1λ. For OAM mode 2, at fixed observation distance 21λ and a fixed UCA element number 12, simulations for 1.10λ, 1.40λ, 1.70λ, 1.80λ, and 2.00λ UCA radii have been conducted. Figures 10(ii) and 10(i) show the electric field phase distribution patterns and normalized radiation patterns for a = 1.10λ, 1.40λ, 1.70λ, 1.80λ, and 2.0λ, respectively.

At a = 1.10λ, side lobes were absent from the NRP, shown in Figs. 10(i)(a) and Figure 10(ii)(a) showed the perfect double twisted configuration of the EFPDP. When the UCA radius was extended to larger than 1.7, side lobes were seen in the NRP (Figure 10(i)(e)). The presence of side lobes is shown by the deepest blue colour ring in NRP at a = 1.80λ (Figure 10(i)(d)). In NRP, the outer area of that ring indicates the side lobes at a = 2.0λ shown in Figure 10(i)(e). Distortions in the spirals pattern indicate the appearance of side lobes in the phase distribution pattern. Minimal distortions are seen at the outer spiral of the EFPDP at a = 1.8λ (Figure 10(ii)(d)). Visible distortions are seen at the outer spiral of the EFPDP at a = 2.0λ (Figure 10(ii)(e)).

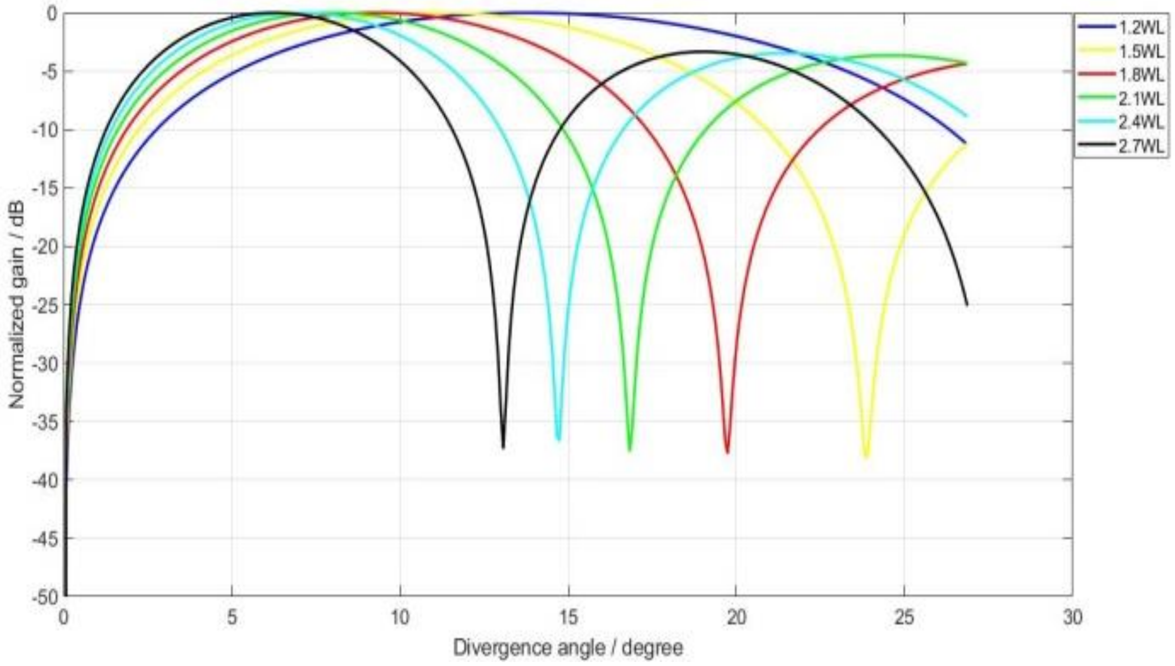

Figure 9. OAM mode 1 radiation patterns at distinct radii.

DOI: https://doi.org/10.52756/ijerr.2023.v36.027

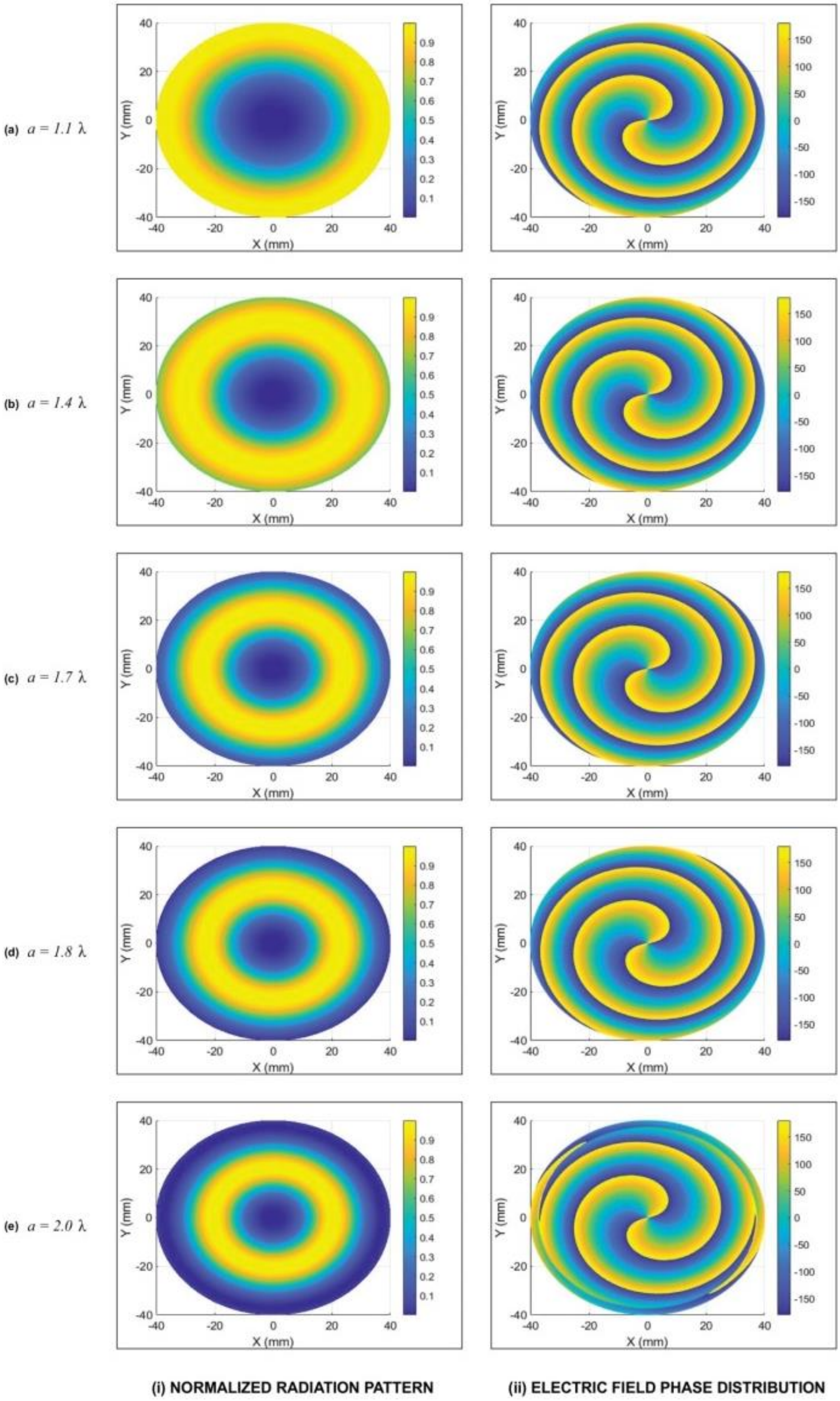

Figure 10. For OAM mode 2, NRP and EFPDP at distinct UCA radii.

DOI: https://doi.org/10.52756/ijerr.2023.v36.027

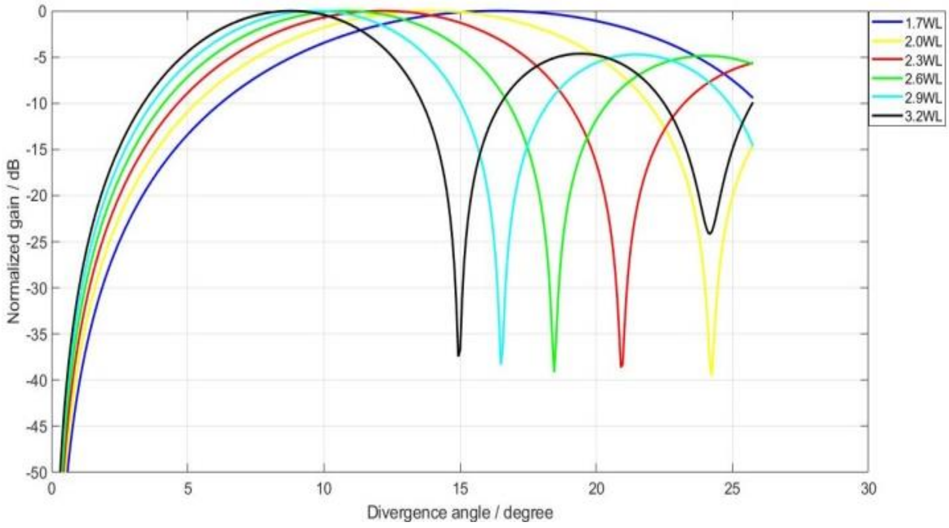

Figure 11. OAM mode 2 radiation patterns at distinct radii.

The influence of radius on radiation patterns is examined using a minimum 12-element UCA since N= 12 is the lowest number of array elements needed to generate ripple-free OAM mode 2. It was noted in the simulation that side lobes did not form until $a = 1.7\lambda$. So 1.7λ was considered as the beginning point. Using a step size of 0.3λ, observations were made up until $a = 3.2\lambda$. The outcomes are displayed in Figure 11. The divergence angle corresponding to the smallest UCA radius (a = 1.7λ) occurred at about 25.752 degrees, as seen by the blue line in Figure 11, and at this radius, there were no side lobes.

A deep curve, indicated by the yellow line, representing a side lobe was discovered at $a = 2.0\lambda$. It was found that the divergence angle decreases as the radius becomes greater. The divergence angle did not considerably decrease after $a = 2.6\lambda$, although the side lobes increased. Therefore, $a = 2.6\lambda$, at which a divergence angle of nearly 18.502 -degrees is generated, is considered a good stopping point (shown by the green line in Figure 9) for OAM mode 2.

(c) Analysis of UCA Radius for OAM Mode 3

Since all radiation patterns were discovered to be nearly comparable before $a = 1.6\lambda$, along with no side lobes. So, simulations for OAM mode 3 have been initiated at $a = 1.6\lambda$. At fixed observation distance 22λ and a fixed UCA element number 14, simulations for 1.60λ, 1.90λ, 2.20λ, 2.30λ, and 2.50λ UCA radii have been conducted.

At $a = 1.6\lambda$, side lobes were absent from NRP, shown in Figs. 12(i)(a) and figure.12(ii)(a) showed the perfect triple-twisted structure of EFPDP. As the UCA radius was raised to larger than 2.2, side lobes were shown to emerge in the NRP, as shown in Figure 12(i)(e). The presence of side lobes is shown by the deepest blue colour ring in NRP at $a = 2.3\lambda$ (Figure 12(i)(d)). In NRP (Figure 12(i)(e)), the outer area of that ring indicates the side lobes at $a = 2.5\lambda$. The distortions of the spiral pattern indicate the appearance of side lobes in EFPDP. Minimal distortions are seen at the outer spiral of the EFPDP at $a = 2.3\lambda$ (Figure 12(ii)(d)). There were significant distortions at the outside spiral of the EFPDP at $a = 2.5\lambda$ shown in Figure 12(ii)(e).

Radiation patterns are examined for the impact of the radius using a minimum 14-element UCA. In the simulation, side lobes were not noticed until $a = 2.2\lambda$. Thus, 2.2λ is utilized as the initial value. At intervals of 0.3λ, observations were made up to $a = 3.7\lambda$. The results are displayed in Figure 13. The divergence angle corresponding to the shortest UCA radius (a = 2.2λ) occurred at about 24.81 degrees, as seen by the blue line in Figure 13 and at this radius there were no side lobes. A deep curve, indicated by the yellow line, representing a side lobe was discovered at $a = 2.5\lambda$.

It was found that as the radius expanded, the divergence angle shrank. The divergence angle did not considerably decrease after $a = 3.1\lambda$, although the amount of side lobes increased. Therefore, $a = 3.1\lambda$, at which a divergence angle of nearly 19.441 -degrees is generated, can be considered as a good stopping point (shown by the green line in Figure 9) for OAM mode 3.

(d) Analysis of UCA Radius for OAM Mode 4

Since all of the radiation patterns for OAM mode, 4 before $a = 2.10\lambda$ were discovered to be nearly comparable along with no side lobes. So, simulations have been initiated from $a = 2.10\lambda$. At fixed observation distance 22λ and fixed UCA element number 16, simulations have been conducted for 2.10λ, 2.40λ, 2.70λ, 2.80λ, and 3.00λ UCA radii for OAM mode 4.

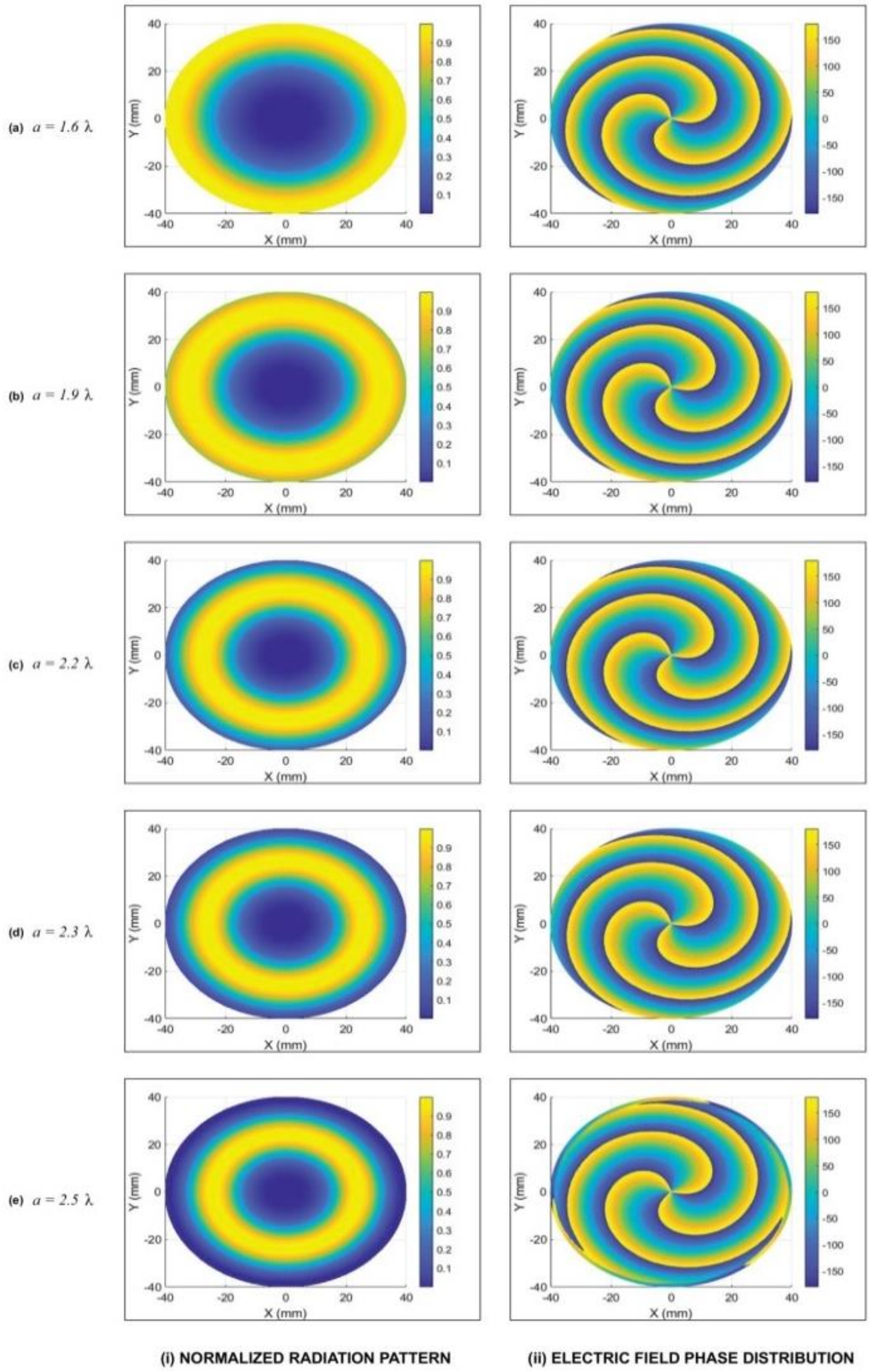

Figure 12. For OAM mode 3, NRP and EFPDP at various UCA radii.

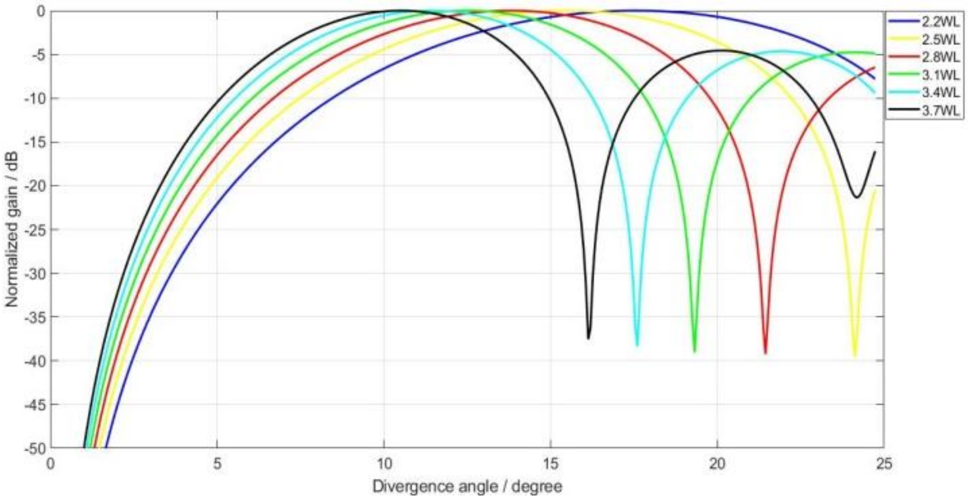

Figure 13. OAM mode 3 radiation patterns at various radii.

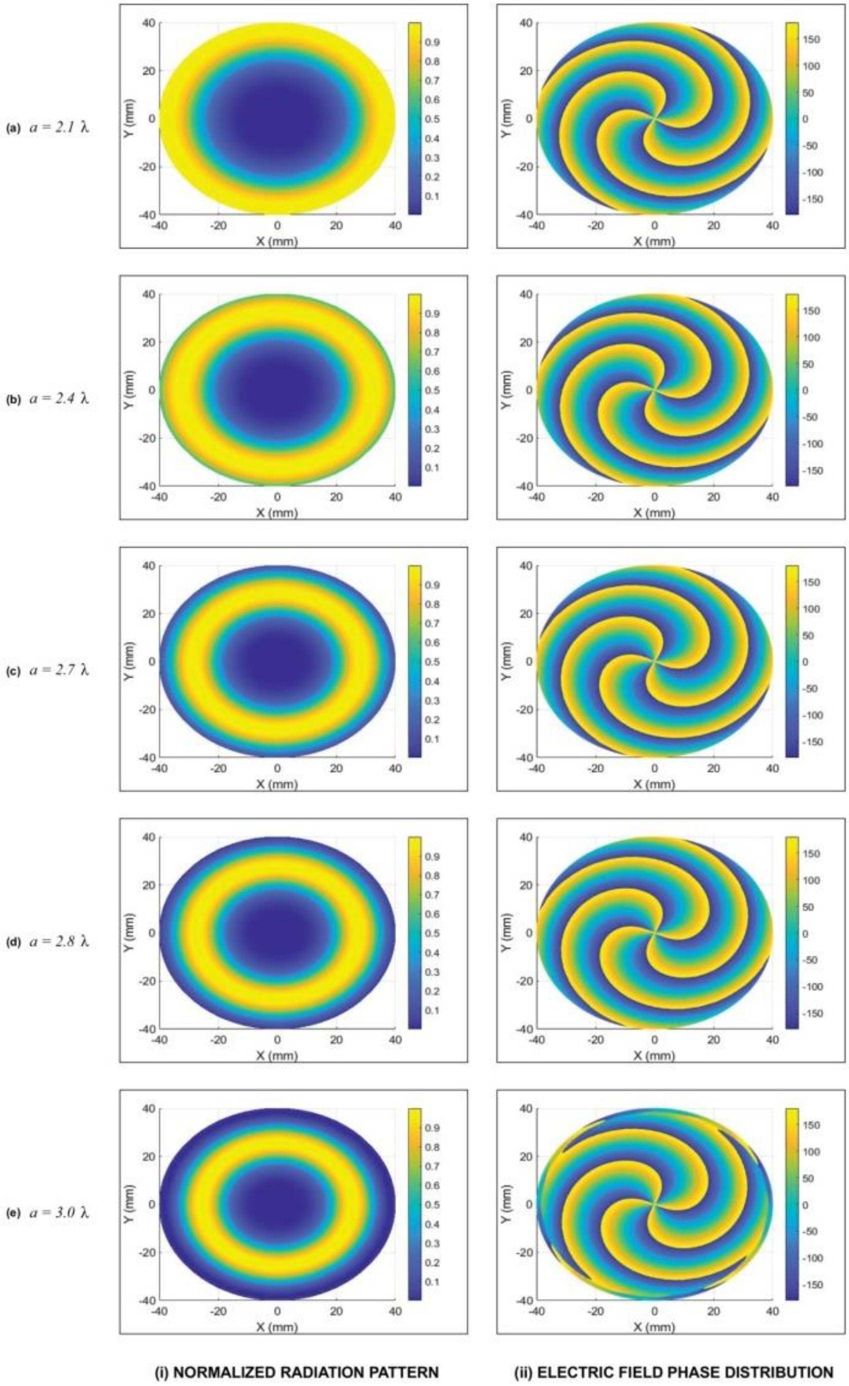

Figure 14. For OAM mode 4, NRP and EFPDP at various UCA radii.

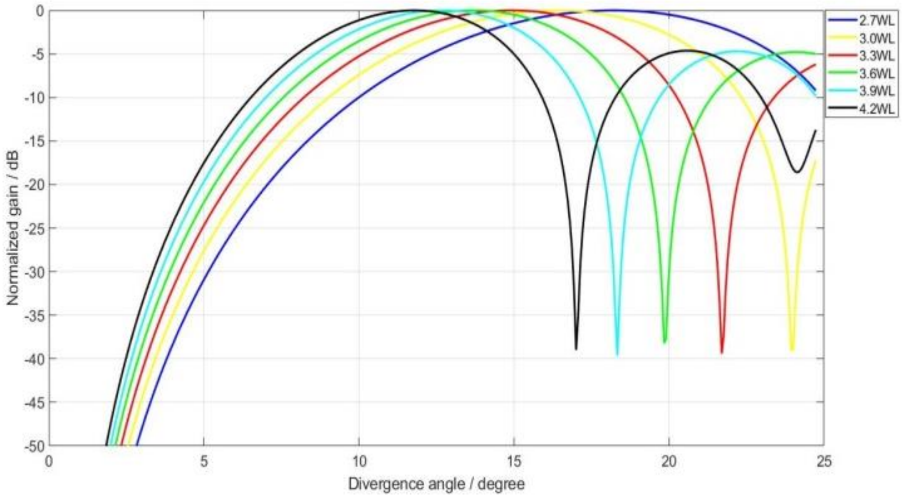

Figure 15. OAM mode 4 radiation patterns at various radii.

A perfect quadruple twisted shape of EFPDP was obtained and side lobes were not evident in NRP at a =2.1λ shown in Figure 14(ii)(a) and Figure 14(i)(a) correspondingly. When the UCA radius was extended to larger than 2.7λ, side lobes were seen in the NRP (Figure 14(i)(e)). A deepest blue color ring in NRP indicates the presence of side lobes at a = 2.8λ (Figure 14(i)(d)). In NRP, the outer area of that ring indicates the side lobes at a = 3.0λ shown in Figure 14(i)(e). The spiral pattern's distortions indicated the side lobes' appearance in EFPDP. Minimal distortions are seen at the outer spiral of the EFPDP at a = 2.8λ (Figure 14(ii)(d)). Visible distortions are seen at the outer spiral of the EFPDP at a = 3.0λ (Figure 14(ii)(e)).

Radiation patterns are examined using a minimum 16-element UCA to determine the impact of UCA radius. In the simulation, side lobes were not noticed until a = 2.7λ. So 2.7λ was considered as the beginning point. At intervals of 0.3λ, observations were made up to a = 4.2λ. The outcomes are displayed in Figure 15. The divergence angle corresponding to the shortest UCA radius (a = 2.7λ) occurred at about 24.81 degrees, as seen by the blue line in Figure 15. A deep curve representing a side lobe was discovered at a = 3.0λ; it is depicted in Figure 15 by the yellow line. It was found that as the radius expanded, the divergence angle became less.

The divergence angle did not considerably decrease after a = 3.6λ, although the side lobes increased. Therefore, a = 3.6λ, at which a divergence angle of about 19.851 degrees was obtained, can be considered as a stopping point (shown by the green line in Figure 15) OAM mode 4.

(e) Analysis of UCA Radius for OAM Mode 5

Since all of the radiation patterns for OAM mode 5 until a =2.60λ were discovered to be nearly comparable along with no side lobes. So, simulations have been initiated from a =2.60λ. At fixed observation distance of 22λ and fixed UCA element number 18, simulations for 2.60λ, 2.90λ, 3.20λ, 3.30λ, and 3.50λ UCA radii have been conducted.

At a = 2.60λ, side lobes were absent from NRP, shown in Figs. 16(i)(a) and fig 16(ii)(b) showed the perfect quintuple twisted shape of EFPDP. When the UCA radius was extended to larger than 3.20λ, side lobes were seen in the NRP (Figure 16(i)(e)). The presence of side lobes is shown by the deepest blue colour ring in NRP at a = 3.30λ (Figure 16(i)(d)). In NRP (Figure 16(i)(e)), the outer area of that ring indicates the side lobes at a = 3.50λ. Spiral pattern distortions indicate the appearance of side lobes in EFPDP. Minimal distortions are seen at the outer spiral of the EFPDP at a = 3.30λ (Figure 16(ii)(d)). Visible distortions were seen at the outer spiral of the EFPDP at a = 3.5λ shown in Figure 16(ii)(e).

Radiation patterns are examined for the impact of the radius using a minimum 18-element UCA. Side lobes did not emerge in the simulation until a = 3.2λ. So 3.2λ is utilized as the initial value. With a step of 0.3λ, observations were made up to a =4.7λ. The outcomes are displayed in Figure 17.

The divergence angle corresponding to the shortest UCA radius (a = 3.2λ) occurred at about 24.81 degrees, as seen by the blue line in Figure 17. A deep curve, indicated by the yellow line, representing a side lobe was discovered at a = 3.5λ. It was found that as the radius expanded, the divergence angle shrank. The divergence angle did not considerably decrease after a = 4.1λ, although the amount of side lobes increased. Therefore, a = 4.1λ, at which a divergence angle of about 20.101 degrees is obtained, can be considered as a satisfactory stopping point (shown by the green line in Figure 17) OAM mode 5.

Approximation and Analysis of Observational Distance for Optimized OAM Modes

The distance between the observation and UCA planes is called the observational distance. “A good line of sight and correct alignment between the transmitting and observing ends are required for the UCA-OAM system” (Fang and Henderson, 2019b). The variations in observational distance and their impact on mode purity have been investigated as this paper's third parameter. Using MATLAB simulation software, a method has been developed to verify the observational distance value needed for a particular OAM mode with reduced divergence and better purity.

(a) OAM Mode 1 observational distance Analysis

“The value of z for far-field conditions should be significantly greater than a" (Fang et al., 2017). It is feasible to show the outcomes and how the radiation patterns will alter if the far field condition is not satisfied. Therefore, simulations started from a small value of observational distance z = 10λ. For OAM mode 1, simulations have been conducted at a fixed UCA radius of 1.20λ for the observational distances of 10λ, 35λ, 45λ, 50λ, and 55λ for OAM mode 1. Figures 18(ii) and 18(i) show the phase distribution patterns and radiation patterns for z = 10λ, 35λ, 45λ, 50λ, and 55λ, respectively. Side lobes were found at z = 10λ in NRP, as illustrated in Figure 18(i)(a). The presence of side lobes is indicated by the dark blue ring in NRP and the outside area of ring in NRP. The middle spirals of single twisted

DOI: https://doi.org/10.52756/ijerr.2023.v36.027

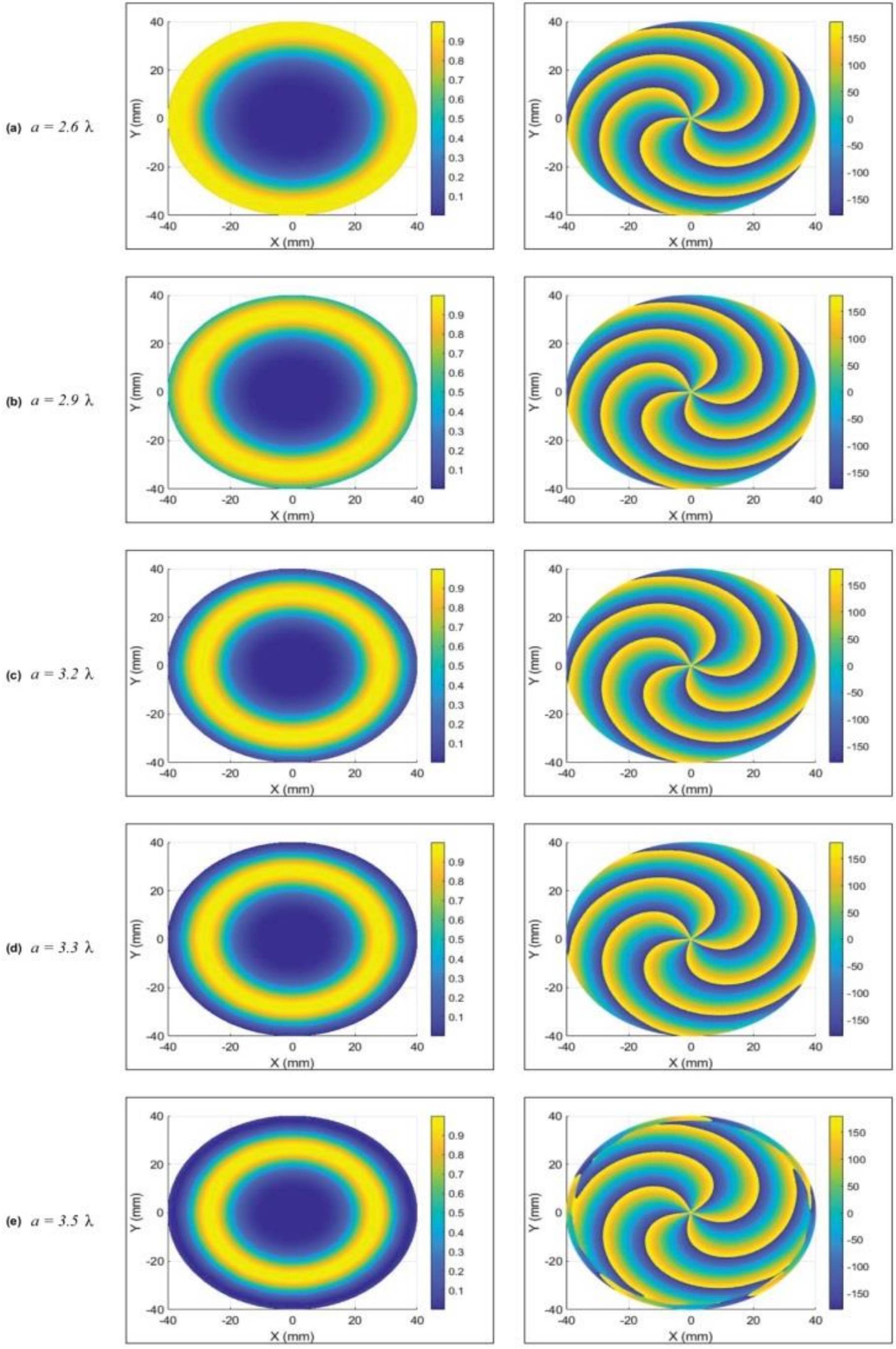

(i) NORMALIZED RADIATION PATTERN (ii) ELECTRIC FIELD PHASE DISTRIBUTION

Figure 16. For OAM mode 5, NRP and EFPDP at various UCA radii.

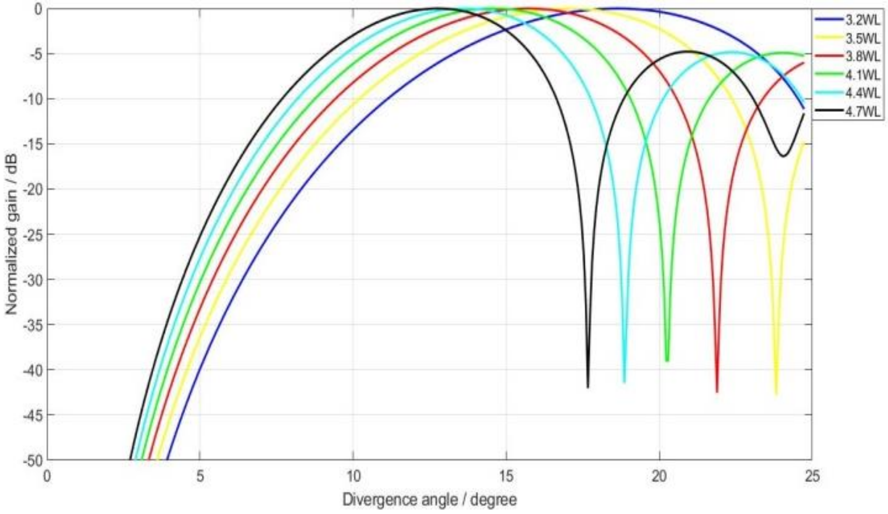

Figure 17. OAM mode 5 radiation patterns at various radii.

DOI: https://doi.org/10.52756/ijerr.2023.v36.027

EFPDP were clearly deformed shown in Figure 18(ii)(a). It was found that the radiation patterns' intensity increased as the value "z" increased. NRP with maximum intensity was observed at z = 35λ indicated in Figure 18(i)(b) by yellow ring. Figure 18(ii)(b) displays the single twisted EFPDP without any distortion, while Figures 18(i)(c) and 18(ii)(c) display the NRP and EFPDP for z = 45λ, respectively.

Further increase in the value of 'z' was observed to cause the radiation patterns' intensity to gradually decrease after z = 35λ. Changes in NRP and EFPDP were essentially minimal after z = 50λ (Figure 18(i)(d) and Figure 18(ii)(d) correspondingly).

For OAM mode 1, the observation distance effect on the radiation pattern is determined using a minimum 8-element UCA. Through simulation, it has been observed that the radiation pattern at z = 35λ had the maximum intensity. Therefore z = 35λ was considered as the beginning point. At 5λ steps, observations were made up to z = 60λ. The findings are displayed in Figure 19. At z = 35λ, the divergence angle of about 16.151 degrees was recorded (blue line in Figure 19). The angle of divergence did not drastically drop after z = 50λ since the radiation pattern showed very little variation after this value. Therefore, z = 50λ (shown by the green line in Figure 19) might be thought of as a good terminating point for appropriate observational distance for OAM mode 1, which provided a divergence angle of about 11.601 degrees.

(b) OAM Mode 2 Observational Distance Analysis

At a given UCA radius of 1.7λ, simulations for the observational distances of 10λ, 30λ, 40λ, 45λ, and 50λ have been conducted for OAM mode 2. Figures 20(ii) and 20(i) have been used to describe the phase distribution patterns and radiation patterns for z = 10λ, 30λ, 40λ, 45λ, and 50λ, respectively.

Side lobes of NRP were found at z = 10λ, which is a little higher than OAM mode 1, shown in Figure 20(i)(a). The centre spirals of double-twisted EFPDP were visibly distorted (Figure 20(ii)(a)). It was found that the radiation patterns' intensity increased as the value "z" increased. Maximum intensity radiation pattern was observed at z = 30λ (shown by a bright yellow ring in Figure 20(i)(b)). Figure 20(ii)(b) shows the double twisted EFPDP in its undistorted state, whereas Figures 20(i)(c) and 20(ii)(c) display the NRP and EFPDP for z = 40λ, respectively. Further increase in the value of 'z' was observed to cause the radiation patterns' intensity to gradually decrease after z = 30λ. Changes in NRP and EFPDP were essentially minimal after z = 45λ (Figs. 20(i)(d) and 20(ii)(d), respectively).

For OAM mode 2, the minimum 12-element UCA is utilized to find out the impact of observation distance on the radiation pattern. The simulation results show that at z = 30λ, the radiation pattern was found with the highest intensity. Thus, 30λ was utilized as the initial value. Observations were made up to z = 55λ with a step of 5λ and outcomes are indicated in Figure 21. The divergence angle value (blue line in Figure 21) obtained at z = 30λ was about 18.751 degrees. The divergence angle did not drastically drop after z = 45λ and the radiation pattern showed very little variation after this value. Therefore, z = 45λ (green line in Figure 21) can be considered as an appropriate observational distance ending point for OAM mode 2, which yielded a divergence angle of about 12.821-degree.

(c) OAM Mode 3 Observational Distance Analysis

For OAM mode 3, simulations for the observational distances of 10λ, 30λ, 35λ, 40λ, and 45λ have been conducted at a fixed UCA radius of 2.2 λ. That is, Figs. 22(ii) and 22(i), respectively, describe the phase distribution patterns and radiation patterns for z = 10λ, 30λ, 35λ, 40λ, and 45λ.

For OAM mode 3, the observation distance influence on the radiation pattern is determined using a minimum 14-element UCA. The simulation results show that at z = 30λ, the radiation pattern with the highest intensity was obtained. Thus, 30λ was utilized as the initial value. Observations were made up to z = 55λ and Figure 23 displays the outcomes. The divergence angle value (shown by the blue line in Figure 23) achieved at z = 30λ, was about 18.651 degrees. The divergence angle did not drastically drop after z = 45λ since the radiation pattern showed very little variation after this value. Therefore, z = 45λ (green line in Figure 23) can be considered as an acceptable terminating point of observational distance for OAM mode 3, which provided a divergence of about 12.701- degrees.

(d) For OAM Mode 4 Observational Distance Analysis

At a given UCA radius of 2.7λ, simulations for the observational distances of 10λ, 20λ, 30λ, 35λ, and 40λ have been conducted for OAM mode 4. Figure 24(ii) and Figure 24(i) provide the phase distribution patterns and radiation patterns for z = 10λ, 20λ, 30λ, 35λ, and 40λ, respectively.

Side lobes of NRP were found at z = 10λ, which is a little higher than OAM mode 3, shown in Figure 20(i)(a). The inner and outer spirals of quadruple twisted EFPDP were visibly distorted (more so than OAM mode 3) (Figure 24(ii)(a)). Figures 24(i)(b) and 24(ii)(b) display the NRP and EFPDP for z = 20λ, respectively. It was

DOI: https://doi.org/10.52756/ijerr.2023.v36.027

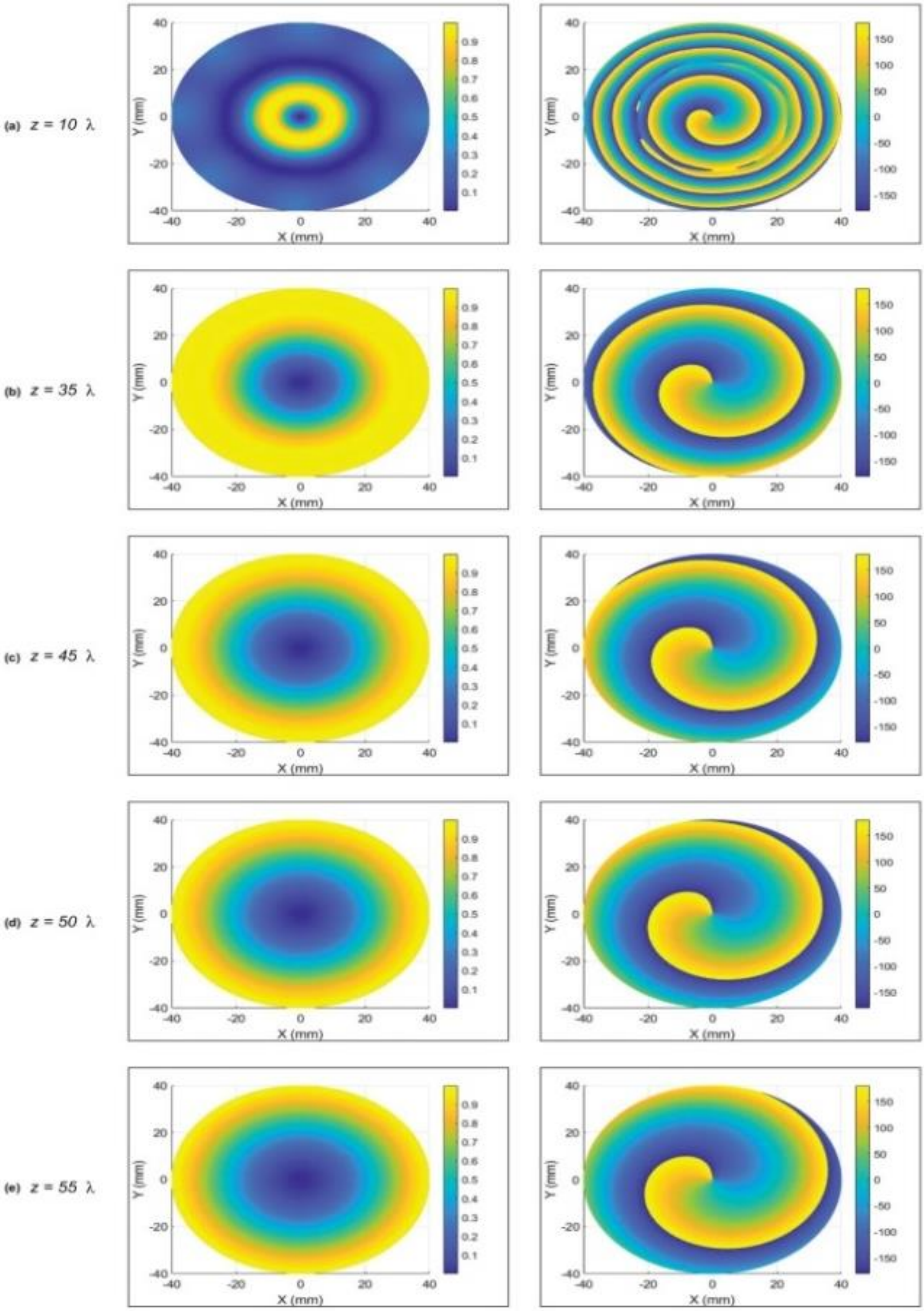

(i) NORMALIZED RADIATION PATTERN **(ii) ELECTRIC FIELD PHASE DISTRIBUTION**

Figure 18. NRP and EFPDP for OAM mode 1 at distinct distances.

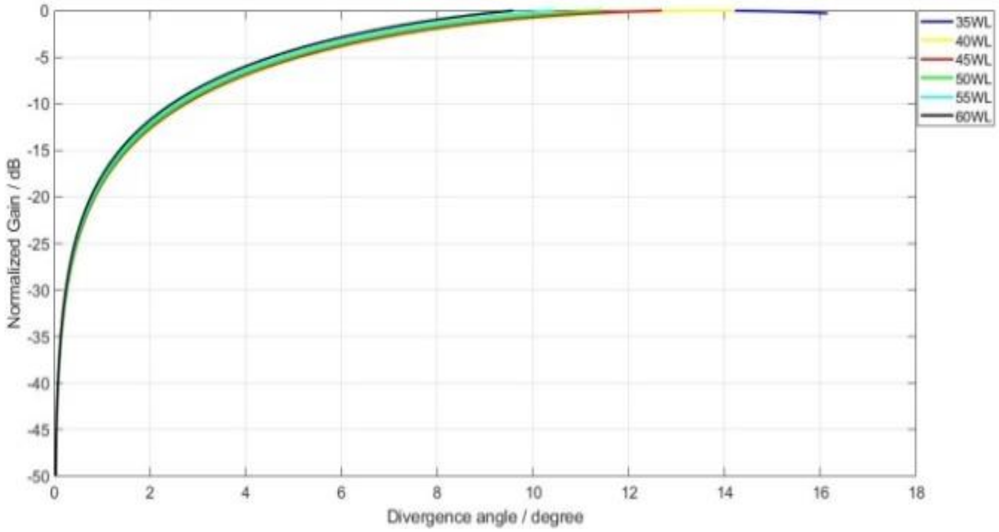

Figure 19. OAM mode 1 radiation patterns at various distances.

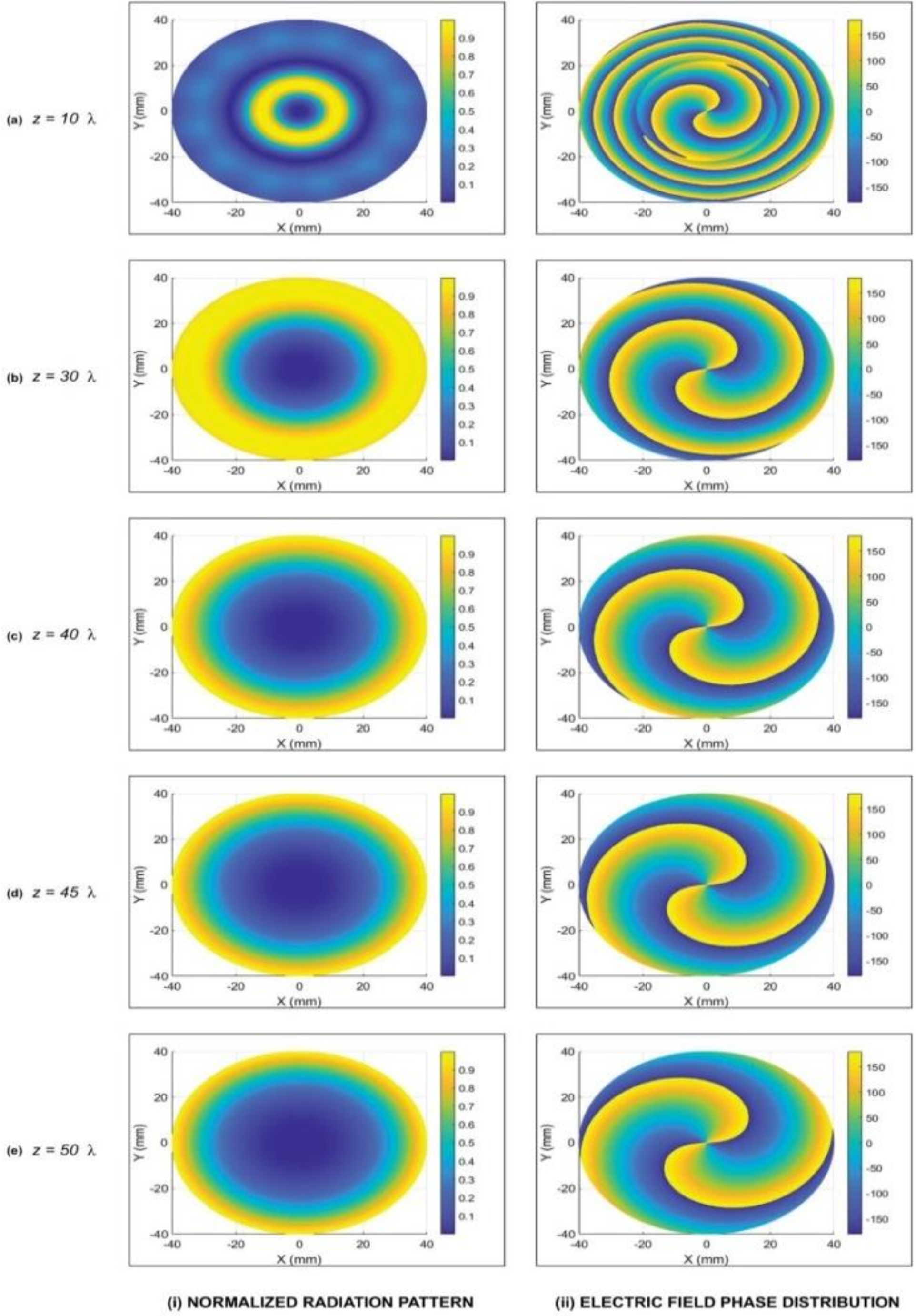

Figure 20. NRP and EFPDP for OAM mode 2 at distinct distances.

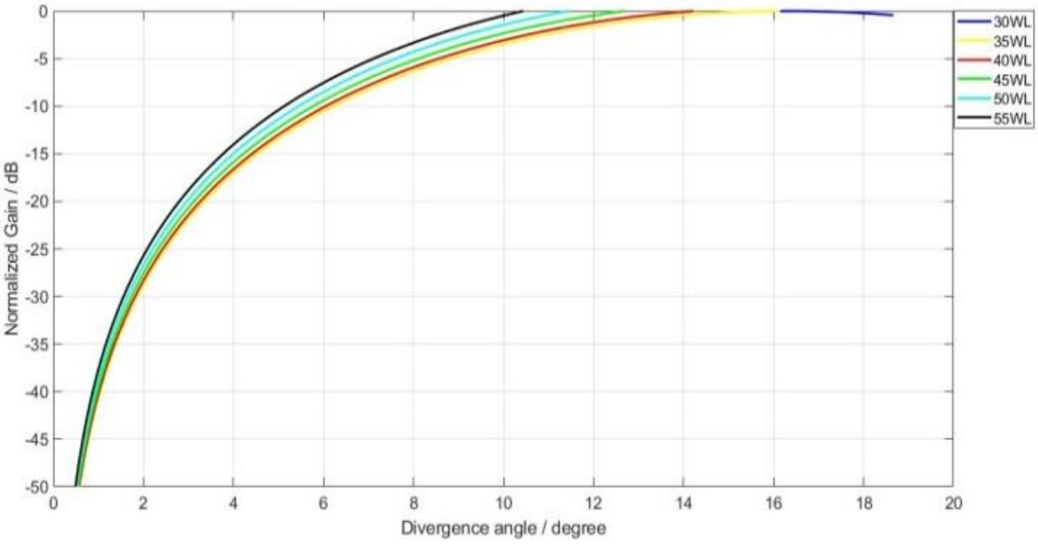

Figure 21. OAM mode 2 radiation patterns at various distances.

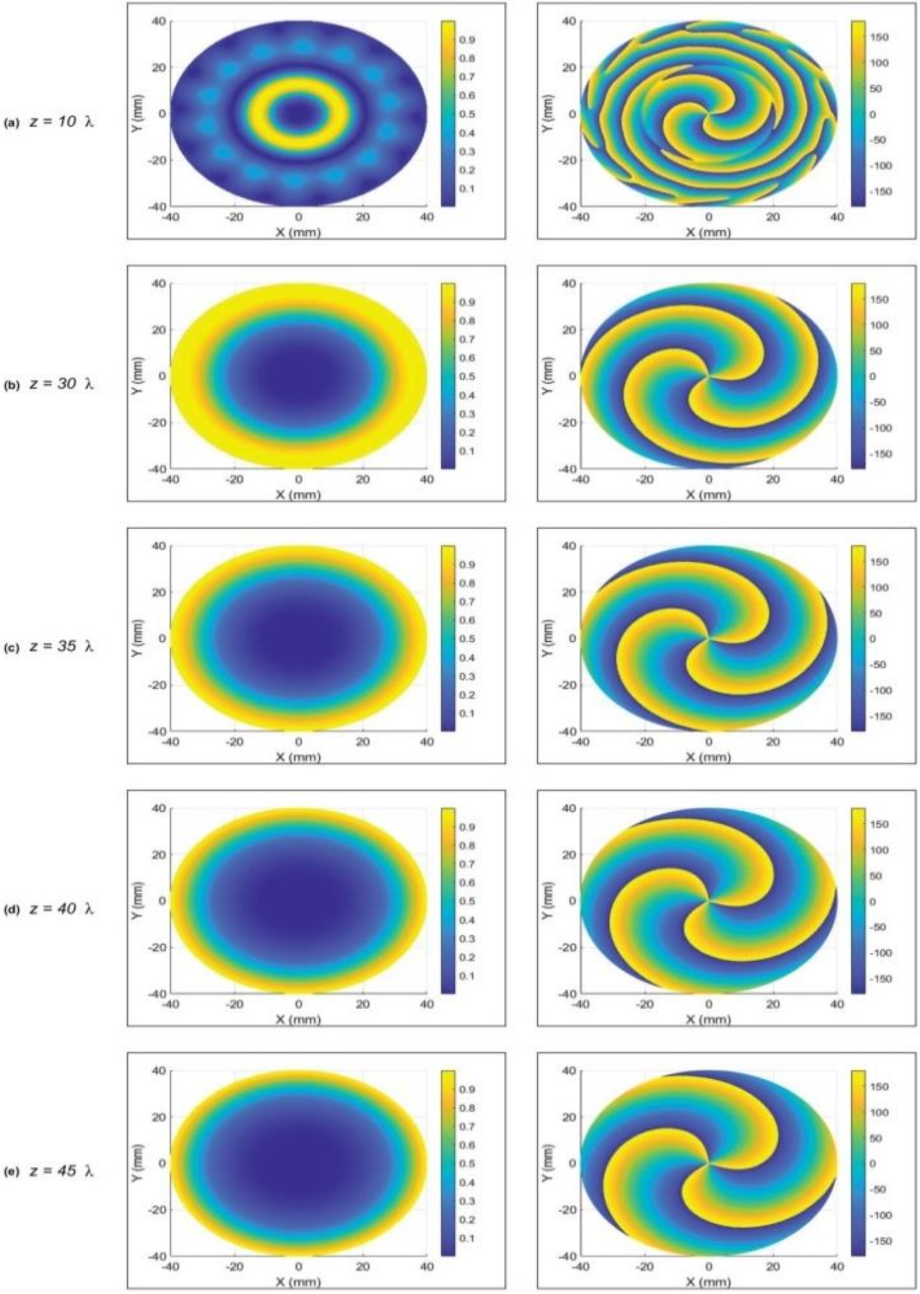

(i) NORMALIZED RADIATION PATTERN (ii) ELECTRIC FIELD PHASE DISTRIBUTION

Figure 22. NRP and EFPDP for OAM mode 3 at distinct distances.

DOI: https://doi.org/10.52756/ijerr.2023.v36.027

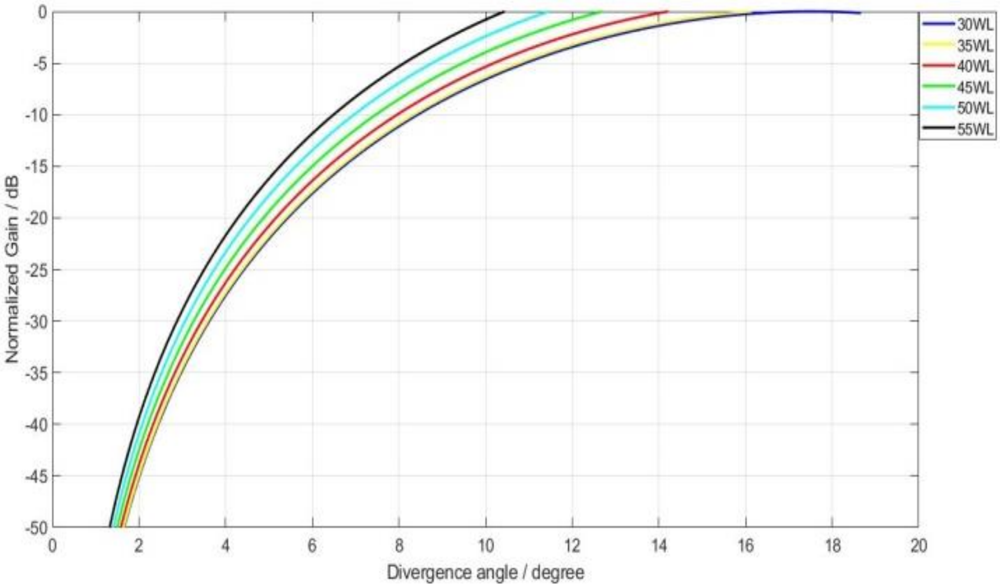

Figure 23. OAM mode 3 radiation patterns at various distances.

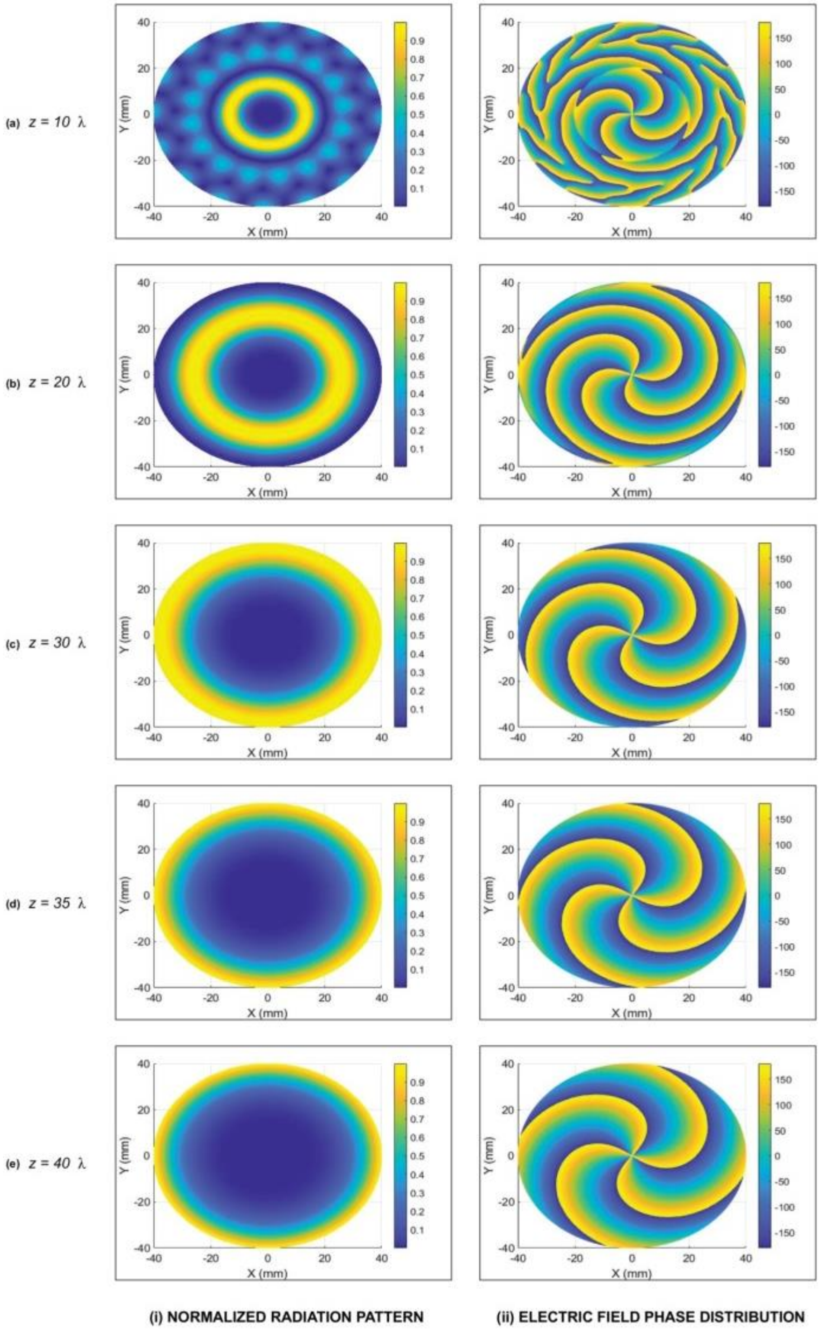

Figure 24. NRP and EFPDP for OAM mode 4 at distinct distances.

DOI: https://doi.org/10.52756/ijerr.2023.v36.027

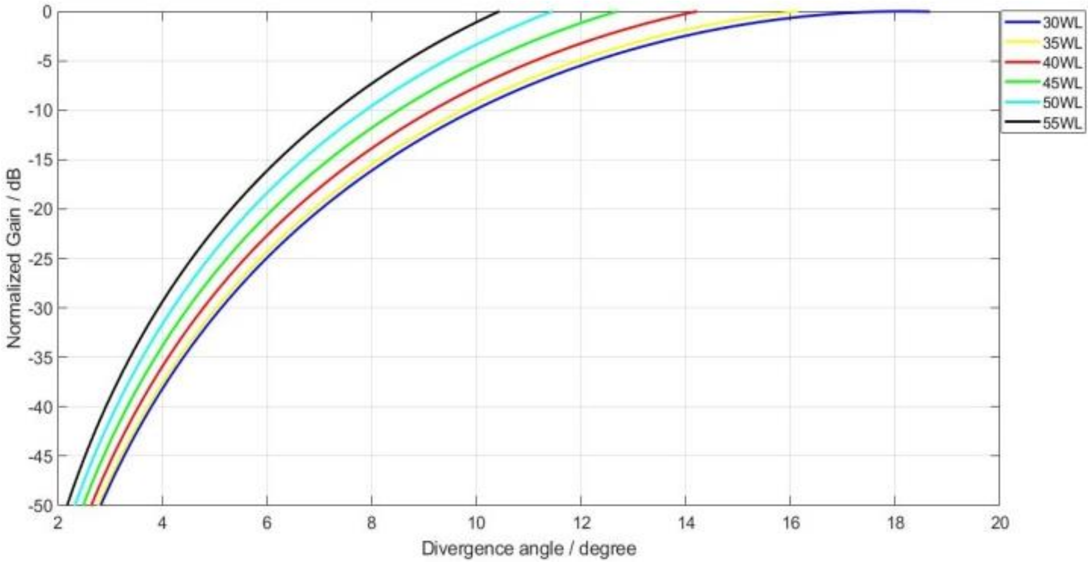

Figure 25. OAM mode 4 radiation patterns at various distances.

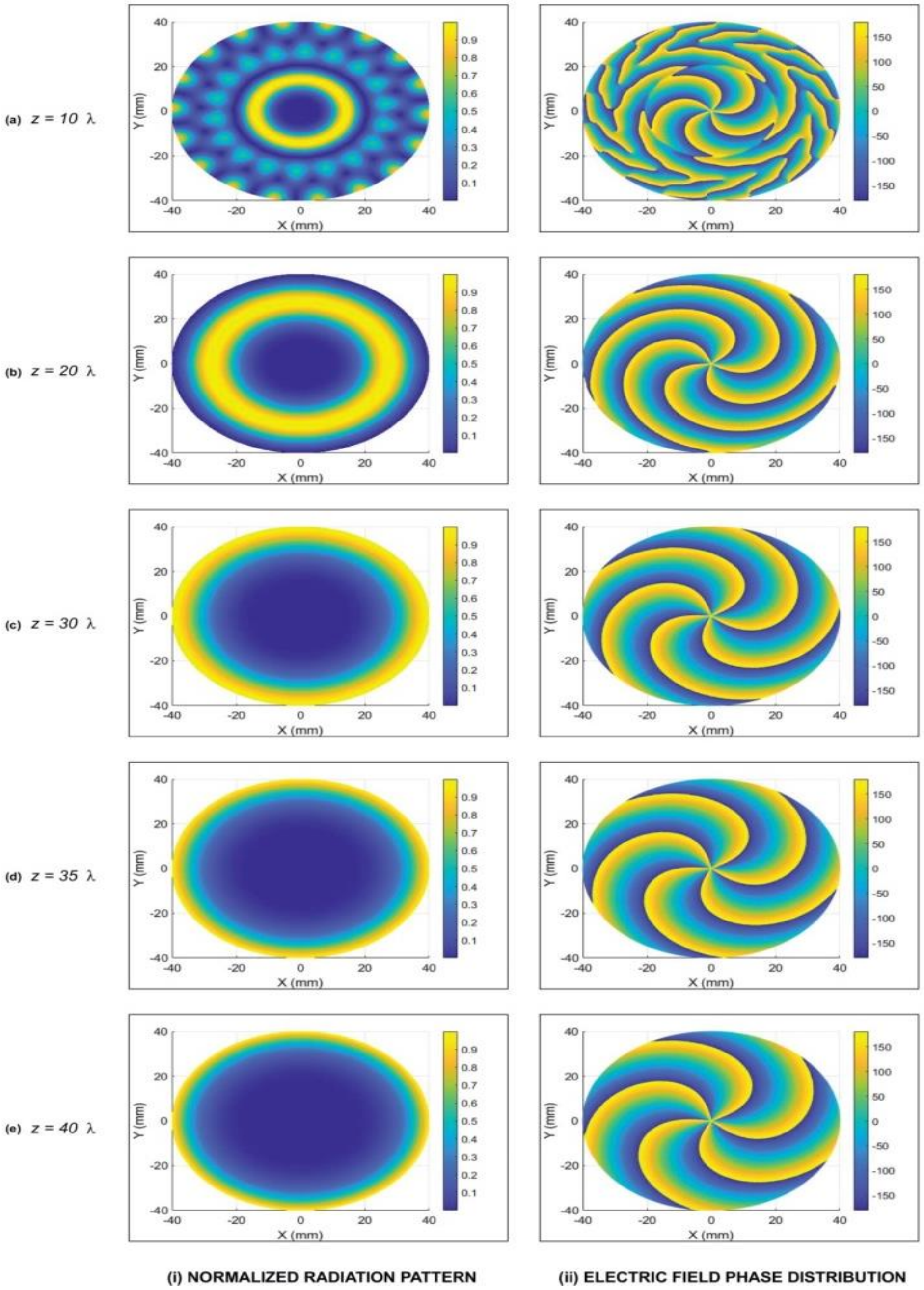

Figure 26. NRP and EFPDP for OAM mode 5 at distinct distances.

found that the radiation patterns' intensity increased as the value "z" increased. NRP’s absolute ring structure forms with maximum intensity at $z = 30\lambda$ (shown by a yellow ring in Figure 24(i)(c)).

At $z=30\lambda$, the quadruple twisted EFPDP is seen in Figure 24(ii)(c)) without any distortion.

It was observed that the radiation patterns' intensity started to decrease slightly after $z = 30\lambda$ with the additional rise in 'z'. Variation in NRP and EFPDP were essentially minimal after $z = 35\lambda$ shown in Figs. 24(i)(d) and 24(ii)(d) respectively.

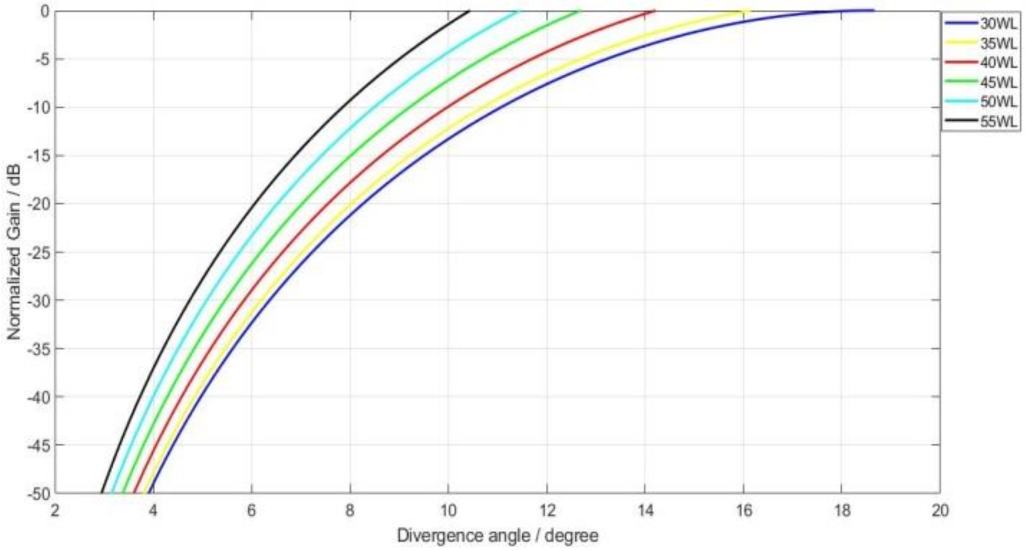

Figure 27. OAM mode 5 radiation patterns at various distances.

For OAM mode 4, the influence of observation distance on the radiation pattern is determined using a minimum 16-element UCA. The simulation results show that at $z = 30\lambda$, the radiation pattern with the highest intensity was obtained. Thus, 30λ was utilized as the initial value. Observations were made up to $z = 55$, and Figure 25 displays the outcomes. The divergence angle value (blue line in Figure 25) was achieved at $z = 30\lambda$, about 18.651 degrees. The divergence angle did not drastically drop after $z = 45\lambda$ since the radiation pattern showed very little variation after this value. Therefore, $z = 45\lambda$ (green line in Figure 25) might be considered as an appropriate ending point of observational distance for OAM mode 4, which provided a divergence of about 12.601 degrees.

(e) For OAM Mode 5 Observational Distance Analysis

At a fixed UCA radius of 3.2λ, simulations for the observational distances of 10λ, 20λ, 30λ, 35λ, and 40λ have been conducted for OAM mode 5. Figure 26(ii) and Figure 26(i) provide descriptions of the phase distribution patterns and radiation patterns for $z = 10\lambda$, 20λ, 30λ, 35λ, and 40λ, respectively.

As can be observed in Figure 26(i)(a), the side lobes of NRP were discovered at $z = 10\lambda$, which is a little bit higher than OAM mode 4. In the intermediate and outer spirals, the quintuple-twisted EFPDP was visibly distorted (more so than OAM mode 4) (Figure 26(ii)(a)). Figures 26(i)(b) and 26(ii)(b) display the NRP and EFPDP for $z = 20\lambda$, respectively. It was found that the radiation patterns' intensity increased as the value "z" increased. For OAM mode 5, the observation distance effect on the radiation pattern is determined using a minimum 18-element UCA. The simulation results show that at $z = 30\lambda$, the radiation pattern with the highest intensity was reached. Thus, 30λ was utilized as the initial value. Observations were made up to $z = 55$, and Figure 27 displays the findings. The divergence angle value (shown by the blue line in Figure 27) occurred at $z = 30\lambda$, was about 18.652 degrees, and it did not considerably decrease after $z = 45\lambda$. Therefore, $z = 45\lambda$ (green line in Figure 27) might be taken as an appropriate ending point observational distance for OAM mode 5, which provided a divergence angle of about 12.602 degrees.

Results and Discussion

Simulation results have been analysed in order to approximate the main parameters, including the number of UCA elements, the UCA radius, and the variation in the observational distance for a particular improved OAM mode, under the subsequent subsections.

A. Approximated values of UCA elements number for optimized OAM modes

The outcomes of separately simulating the UCA element number "N" for OAM modes 1 to 5 are combined in Table 2.

Table 2. UCA Elements Required For Ripple Free Radiation Pattern.

OAM mode (l)	Observational distance (z)	radius of UCA (a)	UCA elements no. (N)
1	20λ	1.20λ	8
2	21λ	1.70λ	12
3	22λ	2.20λ	14
4	22λ	2.70λ	16
5	22λ	3.20λ	18

Table 2 shows the total number of UCA elements required to create patterns of radiation without any ripples. For OAM mode 1, N = 8, N = 12 for mode 2, N = 14, N = 16 for mode 4, and N = 18 for mode 5.B.

B. Approximated values of UCA Radius for OAM Modes

The outcomes of separately simulating the UCA radius "a" for OAM modes 1 to 5 are combined in Table 3.

Table 3 displays the divergence angle values at the "no side lobes" (the UCA radius value below which no side lobes are present), at the "stopping point"(the UCA radius value at which the divergence angle remains relatively constant while the level side lobes increase) and the variation in divergence angle values between the "no side lobes point" and the "stopping point."

Table 3. Divergence Angle at 'No Side Lobe Point' and 'Stopping Point'.

OAM Mode (l)	Radius of UCA Radius (a)	At no side, lobes point value of Divergence angle (θ)	Radius of UCA (a)	At the stopping point value of Divergence angle (θ)	Divergence angle variation ($\Delta\theta$)
1	1.2 λ	26.751	2.1λ	16.901	9.85
2	1.7 λ	25.752	2.6λ	18.502	7.25
3	2.2 λ	24.81	3.1λ	19.441	5.36
4	2.7 λ	24.81	3.6λ	19.851	4.95
5	3.1 λ	24.81	4.1λ	20.101	4.70

C. Approximated value of Observational Distance for Optimized OAM Modes

The results of separately simulating the observational distance "z" for each of the OAM modes 1 to 5 are combined in Table 4.

Table 4 summarizes the divergence angle values at the "maximum intensity point" (the observational distance at which the maximum intensity of the radiation pattern is achieved), at the "ending point" (the observational distance after which the divergence angle does not significantly change) and the variation in divergence angle values between the "maximum intensity point" and the "ending point."

Table 4. Divergence Angle at Maximum Intensity Point and Ending Point.

OAM Mode (l)	Observational Distance (z)	Divergence angle (θ) at maximum intensity point	Observational Distance (z)	Divergence angle (θ) at ending point	Divergence angle variation ($\Delta\theta$)
1	35λ	16.151	50λ	11.601	4.55
2	30λ	18.751	45λ	12.821	5.93
3	30λ	18.651	45λ	12.701	5.95
4	30λ	18.651	45λ	12.601	6.05
5	30λ	18.652	45λ	12.602	6.05

Conclusion

In order to generate improved OAM waves, a uniform circular antenna array is proposed in this research. The following conclusions are drawn after examining the effects of variation in UCA parameters (number of UCA elements (N), UCA radius (a), and observational distance (z)) on the radiation patterns:

The lowest number of UCA elements needed to generate a ripple-free radiation pattern for OAM modes 1 to 5 should be more than the basic essential. For a given OAM mode, the precise number of UCA elements that would produce a ripple-free radiation pattern could be determined in advance using simulations.

Through selecting the UCA radius attentively, the divergence issue (emerges when OAM modes increase in order) may be substantially alleviated. By predicting the stopping point value of the UCA radius prior to simulation, the mode purity and divergence angle could be coordinated. A stopping point value of UCA radius might result in both decreased mode divergence (since the value of the divergence angle at the "stopping point" is significantly less than the value at the "no side lobes point" for a particular OAM mode) and good mode purity (because no further side lobes are present).

Through simulations, less mode divergence with good mode purity might be accomplished by anticipating the observational distance's ending point value. For a certain OAM mode, the divergence angle at the "ending point" is substantially less than the divergence angle at the "maximum intensity point." The reason for the good mode purity in this case is that, despite the radiation pattern's intensity not decreasing significantly from the "maximum intensity point" to the "ending point," there has been a notable increase in the value of "z."

Furthermore, it may be stated that the highest value of "z", up to which a correct alignment between the transmitters and the observing end can be maintained, can be determined by predicting the "ending point."

Conflict of Interest

The authors declare no conflict of interest.

References

Albreem, M. A. M. (2015). 5G wireless communication systems: Vision and challenges. In Proc. Int. Conf. Comput., Commun., Control Technol. (I4CT), Kuching, Malaysia, Apr. 2015, pp. 493-497. https://doi.org/10.1109/I4CT.2015.7219627

Bai, Q., Tennant, A., & Allen, B. (2014). Experimental circular phased array for generating OAM radio beams. *Electronics Letters*, *50*(20), 1414–1415. https://doi.org/10.1049/el.2014.2860

Chen, M. L. N., Jiang, L. J., & Sha, W. E. I. (2018). Orbital angular momentum generation and detection by Geometric-Phase based metasurfaces. *Applied Sciences*, *8*(3), 362. https://doi.org/10.3390/app8030362

Chen, *R.*, Zhou, H., Moretti, M., Wang, X., & Li, J. (2019). Orbital Angular Momentum Waves: Generation, Detection and Emerging Applications. *Physics.app-ph*, *1*(1), 91–106. https://arxiv.org/pdf/1903.07818.pdf

Fang, L., & Henderson, R. M. (2019a). Uniform Millimeter-Wave OAM Dipole Array with Reflector. Paper presented at 2019 ICC-OAM workshop, Shanghai, China. https://doi.org/10.1109/ICCW.2019.8756896

Fang, L., & Henderson, R. M. (2019b). Uniform Circular Array Factor Techniques to Optimize Orbital Angular Momentum Modes Designed With Dipole Antennas at E-band. Presented at 49th European Microwave Conf., Paris, France, 1-3 Oct. 2019, pp. 149- 152. https://doi.org/10.23919/EuMC.2019.8910954

Fang, L., Yao, H., & Henderson, R. M. (2017). OAM antenna arrays at E-band. 2017 IEEE MTT-S International Microwave Symposium (IMS), Honolulu, HI, 2017, pp. 658-661. https://doi.org/10.1109/MWSYM.2017.8058655

Guo, Z., & Yang, G. (2017). Radial uniform circular antenna array for Dual-Mode OAM communication. *IEEE Antennas and Wireless Propagation Letters*, *16*, 404–407. https://doi.org/10.1109/lawp.2016.2581204

Hassan, M. H., Al-Mulla, M., Sievert, B., Rennings, A., & Erni, D. (2020). Evaluation of different phased array approaches for orbital angular momentum beam steering, in 13th German Microw. Conf. (GeMiC 2020), Cottbus, Germany, 2020, pp. 1-4.

Hassan, M. H., Sievert, B., Svejda, J. T., Ahmed, A. M., Barowski, J., Rennings, A., Rolfes, I., Sezgin, A., & Erni, D. (2021). Beam divergence reduction of vortex waves with a tailored lens and a tailored reflector. *IEEE Access*, *9*, 9800–9811. https://doi.org/10.1109/access.2021.3050043

Isakov, D., Wu, Y., Allen, B., Grant, P. S., Stevens, C., & Gibbons, G. J. (2020). Evaluation of the Laguerre–Gaussian mode purity produced by three-dimensional-printed microwave spiral phase plates. *Royal Society Open Science*, *7*(7), 200493. https://doi.org/10.1098/rsos.200493

Li, C., Wang, H., & Hao, Z. (2014). Generation of Electromagnetic Waves with Arbitrary Orbital Angular Momentum Modes. *Scientific Reports*, *4*(1). https://doi.org/10.1038/srep04814

Mohammadi, S. M., Daldorff, L. K. S., Bergman, J., Karlsson, R., Thidé, B., Forozesh, K., Carozzi, T. D., & Isham, B. (2010). Orbital Angular Momentum in Radio—A System Study. *IEEE Transactions on Antennas and Propagation*, *58*(2), 565–572. https://doi.org/10.1109/tap.2009.2037701

Turnbull, G. A., Robertson, D. A., Smith, G., Allen, L. J., & Padgett, M. J. (1996). The generation of free-space Laguerre-Gaussian modes at millimetre-wave frequencies by use of a spiral phaseplate. *Optics Communications*, *127*(4–6), 183–188. https://doi.org/10.1016/0030-4018(96)00070-3

Xu, J., Guo, Y., Yang, P., Zhang, R., Zhai, X., Huang, S., & Bi, K. (2020). Recent progress on RF orbital angular momentum antennas. *Journal of Electromagnetic Waves and Applications*, *34*(3), 275–300. https://doi.org/10.1080/09205071.2019.1708814

Yao, H. et al. (2017). Experimental Demonstration of a Dual-channel E-band Communication Link using Commercial Impulse Radios with Orbital Angular Momentum Multiplexing. Presented at the 2017 IEEE RWS, Phoenix, AZ, Jan. 15-18, 2017. https://doi.org/10.1109/RWS.2017.7885943

Yu, S., Li, L., Shi, G., Zhu, C., & Shi, Y. (2016). Generating multiple orbital angular momentum vortex beams using a metasurface in radio frequency domain. *Applied Physics Letters*, *108*(24). https://doi.org/10.1063/1.4953786

How to cite this Article:

Rakhee, Rajesh Bhadada and Usha (2023). High Purity Orbital Angular Momentum Modes Reconfiguration Using Uniform Circular Array Antenna to Enhance Channel Capacity and Spectral Efficiency. *International Journal of Experimental Research and Review*, *36*, 285-310.

DOI : https://doi.org/10.52756/ijerr.2023.v36.027